Measurement of $b\bar{b}$ rapidity correlations in $p\bar{p}$ collisions at $\sqrt{s}=1.8$ TeV

F. Abe,[17] H. Akimoto,[39] A. Akopian,[31] M. G. Albrow,[7] A. Amadon,[5] S. R. Amendolia,[27] D. Amidei,[20] J. Antos,[33] S. Aota,[37] G. Apollinari,[31] T. Arisawa,[39] T. Asakawa,[37] W. Ashmanskas,[5] M. Atac,[7] P. Azzi-Bacchetta,[25] N. Bacchetta,[25] S. Bagdasarov,[31] M. W. Bailey,[22] P. de Barbaro,[30] A. Barbaro-Galtieri,[18] V. E. Barnes,[29] B. A. Barnett,[15] M. Barone,[9] G. Bauer,[19] T. Baumann,[11] F. Bedeschi,[27] S. Behrends,[3] S. Belforte,[27] G. Bellettini,[27] J. Bellinger,[40] D. Benjamin,[35] J. Bensinger,[3] A. Beretvas,[7] J. P. Berge,[7] J. Berryhill,[5] S. Bertolucci,[9] S. Bettelli,[27] B. Bevensee,[26] A. Bhatti,[31] K. Biery,[7] C. Bigongiari,[27] M. Binkley,[7] D. Bisello,[25] R. E. Blair,[1] C. Blocker,[3] K. Bloom,[20] S. Blusk,[30] A. Bodek,[30] W. Bokhari,[26] G. Bolla,[29] Y. Bonushkin,[4] D. Bortoletto,[29] J. Boudreau,[28] L. Breccia,[2] C. Bromberg,[21] N. Bruner,[22] R. Brunetti,[2] E. Buckley-Geer,[7] H. S. Budd,[30] K. Burkett,[11] G. Busetto,[25] A. Byon-Wagner,[7] K. L. Byrum,[1] M. Campbell,[20] A. Caner,[27] W. Carithers,[18] D. Carlsmith,[40] J. Cassada,[30] A. Castro,[25] D. Cauz,[36] A. Cerri,[27] P. S. Chang,[33] P. T. Chang,[33] H. Y. Chao,[33] J. Chapman,[20] M. -T. Cheng,[33] M. Chertok,[34] G. Chiarelli,[27] C. N. Chiou,[33] F. Chlebana,[7] L. Christofek,[13] R. Cropp,[14] M. L. Chu,[33] S. Cihangir,[7] A. G. Clark,[10] M. Cobal,[27] E. Cocca,[27] M. Contreras,[5] J. Conway,[32] J. Cooper,[7] M. Cordelli,[9] D. Costanzo,[27] C. Couyoumtzelis,[10] D. Cronin-Hennessy,[6] R. Culbertson,[5] D. Dagenhart,[38] T. Daniels,[19] F. DeJongh,[7] S. Dell'Agnello,[9] M. Dell'Orso,[27] R. Demina,[7] L. Demortier,[31] M. Deninno,[2] P. F. Derwent,[7] T. Devlin,[32] J. R. Dittmann,[6] S. Donati,[27] J. Done,[34] T. Dorigo,[25] N. Eddy,[13] K. Einsweiler,[18] J. E. Elias,[7] R. Ely,[18] E. Engels, Jr.,[28] W. Erdmann,[7] D. Errede,[13] S. Errede,[13] Q. Fan,[30] R. G. Feild,[41] Z. Feng,[15] C. Ferretti,[27] I. Fiori,[2] B. Flaugher,[7] G. W. Foster,[7] M. Franklin,[11] J. Freeman,[7] J. Friedman,[19] Y. Fukui,[17] S. Gadomski,[14] S. Galeotti,[27] M. Gallinaro,[26] O. Ganel,[35] M. Garcia-Sciveres,[18] A. F. Garfinkel,[29] C. Gay,[41] S. Geer,[7] D. W. Gerdes,[20] P. Giannetti,[27] N. Giokaris,[31] P. Giromini,[9] G. Giusti,[27] M. Gold,[22] A. Gordon,[11] A. T. Goshaw,[6] Y. Gotra,[28] K. Goulianos,[31] H. Grassmann,[36] C. Green,[29] L. Groer,[32] C. Grosso-Pilcher,[5] G. Guillian,[20] J. Guimaraes da Costa,[15] R. S. Guo,[33] C. Haber,[18] E. Hafen,[19] S. R. Hahn,[7] R. Hamilton,[11] T. Handa,[12] R. Handler,[40] W. Hao,[35] F. Happacher,[9] K. Hara,[37] A. D. Hardman,[29] R. M. Harris,[7] F. Hartmann,[16] J. Hauser,[4] E. Hayashi,[37] J. Heinrich,[26] A. Heiss,[16] B. Hinrichsen,[14] K. D. Hoffman,[29] C. Holck,[26] R. Hollebeek,[26] L. Holloway,[13] Z. Huang,[20] B. T. Huffman,[28] R. Hughes,[23] J. Huston,[21] J. Huth,[11] H. Ikeda,[37] M. Incagli,[27] J. Incandela,[7] G. Introzzi,[27] J. Iwai,[39] Y. Iwata,[12] E. James,[20] H. Jensen,[7] U. Joshi,[7] E. Kajfasz,[25] H. Kambara,[10] T. Kamon,[34] T. Kaneko,[37] K. Karr,[38] H. Kasha,[41] Y. Kato,[24] T. A. Keaffaber,[29] K. Kelley,[19] R. D. Kennedy,[7] R. Kephart,[7] D. Kestenbaum,[11] D. Khazins,[6] T. Kikuchi,[37] B. J. Kim,[27] H. S. Kim,[14] S. H. Kim,[37] Y. K. Kim,[18] L. Kirsch,[3] S. Klimenko,[8] D. Knoblauch,[16] P. Koehn,[23] A. Köngeter,[16] K. Kondo,[37] J. Konigsberg,[8] K. Kordas,[14] A. Korytov,[8] E. Kovacs,[1] W. Kowald,[6] J. Kroll,[26] M. Kruse,[30] S. E. Kuhlmann,[1] E. Kuns,[32] K. Kurino,[12] T. Kuwabara,[37] A. T. Laasanen,[29] S. Lami,[27] S. Lammel,[7] J. I. Lamoureux,[3] M. Lancaster,[18] M. Lanzoni,[27] G. Latino,[27] T. LeCompte,[1] S. Leone,[27] J. D. Lewis,[7] M. Lindgren,[4] T. M. Liss,[13] J. B. Liu,[30] Y. C. Liu,[33] N. Lockyer,[26] O. Long,[26] M. Loreti,[25] D. Lucchesi,[27] P. Lukens,[7] S. Lusin,[40] J. Lys,[18] K. Maeshima,[7] P. Maksimovic,[11] M. Mangano,[27] M. Mariotti,[25] J. P. Marriner,[7] G. Martignon,[25] A. Martin,[41] J. A. J. Matthews,[22] P. Mazzanti,[2] K. McFarland,[30] P. McIntyre,[34] P. Melese,[31] M. Menguzzato,[25] A. Menzione,[27] E. Meschi,[27] S. Metzler,[26] C. Miao,[20] T. Miao,[7] G. Michail,[11] R. Miller,[21] H. Minato,[37] S. Miscetti,[9] M. Mishina,[17] S. Miyashita,[37] N. Moggi,[27] E. Moore,[22] Y. Morita,[17] A. Mukherjee,[7] T. Muller,[16] A. Munar,[27] P. Murat,[27] S. Murgia,[21] M. Musy,[36] H. Nakada,[37] T. Nakaya,[5] I. Nakano,[12] C. Nelson,[7] D. Neuberger,[16] C. Newman-Holmes,[7] C.-Y. P. Ngan,[19] L. Nodulman,[1] A. Nomerotski,[8] S. H. Oh,[6] T. Ohmoto,[12] T. Ohsugi,[12] R. Oishi,[37] M. Okabe,[37] T. Okusawa,[24] J. Olsen,[40] C. Pagliarone,[27] R. Paoletti,[27] V. Papadimitriou,[35] S. P. Pappas,[41] N. Parashar,[27] A. Parri,[9] J. Patrick,[7] G. Pauletta,[36] M. Paulini,[18] A. Perazzo,[27] L. Pescara,[25] M. D. Peters,[18] T. J. Phillips,[6] G. Piacentino,[27] M. Pillai,[30] K. T. Pitts,[7] R. Plunkett,[7] A. Pompos,[29] L. Pondrom,[40] J. Proudfoot,[1] F. Ptohos,[11] G. Punzi,[27] K. Ragan,[14] D. Reher,[18] M. Reischl,[16] A. Ribon,[25] F. Rimondi,[2] L. Ristori,[27] W. J. Robertson,[6] A. Robinson,[14] T. Rodrigo,[27] S. Rolli,[38] L. Rosenson,[19] R. Roser,[13] T. Saab,[14] W. K. Sakumoto,[30] D. Saltzberg,[4] A. Sansoni,[9] L. Santi,[36] H. Sato,[37] P. Schlabach,[7] E. E. Schmidt,[7] M. P. Schmidt,[41] A. Scott,[4] A. Scribano,[27] S. Segler,[7] S. Seidel,[22] Y. Seiya,[37] F. Semeria,[2] T. Shah,[19] M. D. Shapiro,[18] N. M. Shaw,[29] P. F. Shepard,[28] T. Shibayama,[37] M. Shimojima,[37] M. Shochet,[5] J. Siegrist,[18] A. Sill,[35] P. Sinervo,[14] P. Singh,[13] K. Sliwa,[38] C. Smith,[15] F. D. Snider,[15] J. Spalding,[7] T. Speer,[10] P. Sphicas,[19] F. Spinella,[27] M. Spiropulu,[11] L. Spiegel,[7] L. Stanco,[25] J. Steele,[40] A. Stefanini,[27] R. Ströhmer,[7,*] J. Strologas,[13] F. Strumia,[10] D. Stuart,[7] K. Sumorok,[19] J. Suzuki,[37] T. Suzuki,[37] T. Takahashi,[24] T. Takano,[24] R. Takashima,[12] K. Takikawa,[37] M. Tanaka,[37] B. Tannenbaum,[4] F. Tartarelli,[27] W. Taylor,[14] M. Tecchio,[20] P. K. Teng,[33] Y. Teramoto,[24] K. Terashi,[37] S. Tether,[19] D. Theriot,[7] T. L. Thomas,[22] R. Thurman-Keup,[1] M. Timko,[38] P. Tipton,[30] A. Titov,[31] S. Tkaczyk,[7] D. Toback,[5] K. Tollefson,[30] A. Tollestrup,[7] H. Toyoda,[24] W. Trischuk,[14] J. F. de Troconiz,[11] S. Truitt,[20] J. Tseng,[19] N. Turini,[27] T. Uchida,[37] F. Ukegawa,[26] J. Valls,[32] S. C. van den Brink,[15] S. Vejcik III,[20] G. Velev,[27] I. Volobouev,[18] R. Vidal,[7] R. Vilar,[7,*] D. Vucinic,[19] R. G. Wagner,[1] R. L. Wagner,[7] J. Wahl,[5] N. B. Wallace,[27] A. M. Walsh,[32] C. Wang,[6] C. H. Wang,[33] M. J. Wang,[33] A. Warburton,[14] T. Watanabe,[37] T. Watts,[32] R. Webb,[34] C. Wei,[6] H. Wenzel,[16] W. C. Wester III,[7] A. B. Wicklund,[1] E. Wicklund,[7] R. Wilkinson,[26] H. H. Williams,[26] P. Wilson,[7] B. L. Winer,[23] D. Winn,[20] D. Wolinski,[20] J. Wolinski,[21] S. Worm,[22] X. Wu,[10] J. Wyss,[27] A. Yagil,[7] W. Yao,[18] K. Yasuoka,[37] G. P. Yeh,[7] P. Yeh,[33] J. Yoh,[7] C. Yosef,[21] T. Yoshida,[24] I. Yu,[7] A. Zanetti,[36] F. Zetti,[27] and S. Zucchelli[2]

(CDF Collaboration)

[1]*Argonne National Laboratory, Argonne, Illinois 60439*
[2]*Istituto Nazionale di Fisica Nucleare, University of Bologna, I-40127 Bologna, Italy*
[3]*Brandeis University, Waltham, Massachusetts 02254*
[4]*University of California at Los Angeles, Los Angeles, California 90024*
[5]*University of Chicago, Chicago, Illinois 60637*
[6]*Duke University, Durham, North Carolina 27708*
[7]*Fermi National Accelerator Laboratory, Batavia, Illinois 60510*
[8]*University of Florida, Gainesville, Florida 32611*
[9]*Laboratori Nazionali di Frascati, Istituto Nazionale di Fisica Nucleare, I-00044 Frascati, Italy*
[10]*University of Geneva, CH-1211 Geneva 4, Switzerland*
[11]*Harvard University, Cambridge, Massachusetts 02138*
[12]*Hiroshima University, Higashi-Hiroshima 724, Japan*
[13]*University of Illinois, Urbana, Illinois 61801*
[14]*Institute of Particle Physics, McGill University, Montreal, Canada H3A 2T8*
and University of Toronto, Toronto, Canada M5S 1A7
[15]*The Johns Hopkins University, Baltimore, Maryland 21218*
[16]*Institut für Experimentelle Kernphysik, Universität Karlsruhe, 76128 Karlsruhe, Germany*
[17]*National Laboratory for High Energy Physics (KEK), Tsukuba, Ibaraki 305, Japan*
[18]*Ernest Orlando Lawrence Berkeley National Laboratory, Berkeley, California 94720*
[19]*Massachusetts Institute of Technology, Cambridge, Massachusetts 02139*
[20]*University of Michigan, Ann Arbor, Michigan 48109*
[21]*Michigan State University, East Lansing, Michigan 48824*
[22]*University of New Mexico, Albuquerque, New Mexico 87131*
[23]*The Ohio State University, Columbus, Ohio 43210*
[24]*Osaka City University, Osaka 588, Japan*
[25]*Universita di Padova, Istituto Nazionale di Fisica Nucleare, Sezione di Padova, I-35131 Padova, Italy*
[26]*University of Pennsylvania, Philadelphia, Pennsylvania 19104*
[27]*Istituto Nazionale di Fisica Nucleare, University and Scuola Normale Superiore of Pisa, I-56100 Pisa, Italy*
[28]*University of Pittsburgh, Pittsburgh, Pennsylvania 15260*
[29]*Purdue University, West Lafayette, Indiana 47907*
[30]*University of Rochester, Rochester, New York 14627*
[31]*Rockefeller University, New York, New York 10021*
[32]*Rutgers University, Piscataway, New Jersey 08855*
[33]*Academia Sinica, Taipei, Taiwan 11530, Republic of China*
[34]*Texas A&M University, College Station, Texas 77843*
[35]*Texas Tech University, Lubbock, Texas 79409*
[36]*Istituto Nazionale di Fisica Nucleare, University of Trieste/Udine, Trieste, Italy*
[37]*University of Tsukuba, Tsukuba, Ibaraki 305, Japan*
[38]*Tufts University, Medford, Massachusetts 02155*
[39]*Waseda University, Tokyo 169, Japan*
[40]*University of Wisconsin, Madison, Wisconsin 53706*
[41]*Yale University, New Haven, Connecticut 06520*

(Received 7 December 1998; published 30 December 1999)

We report the first direct measurement of $b\bar{b}$ rapidity correlations in $p\bar{p}$ collisions at $\sqrt{s}=1.8$ TeV. We select events with a high transverse momentum muon accompanied by a jet, and a second jet associated with a decay vertex displaced from the $p\bar{p}$ interaction vertex. Two independent samples are obtained corresponding to events with a forward ($2.0<|\eta|<2.6$) or central ($|\eta|<0.6$) muon. We measure the ratio of forward to central $b\bar{b}$ production to be $0.361\pm0.033(\text{stat})^{+0.015}_{-0.031}(\text{syst})$, in good agreement with the next-to-leading order QCD prediction $0.338^{+0.014}_{-0.097}$.

PACS number(s): 13.87.Ce, 13.85.Qk

I. INTRODUCTION

The study of $b\bar{b}$ production in high energy $p\bar{p}$ collisions has proven to be a valuable tool for the quantitative testing of perturbative QCD. The b-quark mass is considered large enough ($m_b \gg \Lambda_{\text{QCD}}$) that the production cross section can be expressed as a series expansion in the strong coupling α_s, while the large semileptonic branching fraction and long lifetime of b hadrons provide convenient experimental signatures that serve to separate $b\bar{b}$ production from the large QCD backgrounds at a hadron collider. The majority of

*Visitor.

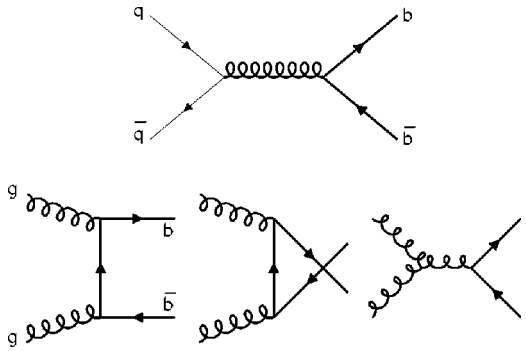

FIG. 1. Lowest order Feynman diagrams for $b\bar{b}$ production.

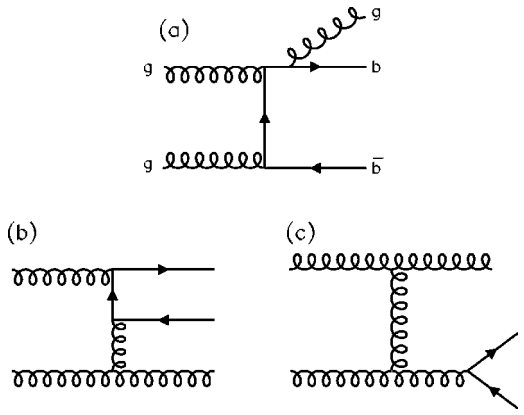

FIG. 2. Representative Feynman diagrams for the (a) direct, (b) flavor excitation, and (c) gluon splitting $b\bar{b}$ production processes.

bottom-production measurements at $p\bar{p}$ colliders have been restricted to the central rapidity region: $|y_b|<1.5$ for the UA1 measurements at CERN, and $|y_b|<1.0$ for the Collider Detector at Fermilab (CDF) and DØ measurements at the Tevatron [1]. Studies in the central region of both single-inclusive transverse-momentum spectra [2–4] and of azimuthal correlations [5–7] have been reported. The comparison of data with next-to-leading-order (NLO) QCD calculations [8–10] reveals a systematic pattern of deviations in the overall production rate, with the shape of all tested distributions agreeing satisfactorily with the theoretical expectations [11]. The excess in the measured production rates over theoretical estimates has been ascribed to various sources, including higher-order corrections and limited understanding of the nonperturbative part of the fragmentation function. It was pointed out in recent studies by two separate groups that modifying the heavy-quark fragmentation function [12], or employing the variable-flavor-number perturbative calculation [13] rather than the fixed-flavor scheme used in Ref. [8,9], not only influences the central production rate, but can also lead to an increase in the relative forward/central inclusive production rate. The study of forward *b*-quark production therefore adds important complementary information to that provided by previous measurements of central production.

The DØ Collaboration was the first to report a forward *b* production measurement at a hadron collider [14]. They identified muons in the rapidity range $2.4<|y|<3.2$ and determined the fraction of muons from *b* decay. The result agrees with the shape of the p_T spectrum predicted by NLO QCD [10], but again with an excess in the measured production rates over theoretical estimates. Our present analysis provides a measurement of the ratio of forward to central $b\bar{b}$ cross sections, using similar data samples and kinematic requirements. Thus, we are able to eliminate or significantly reduce many of the experimental systematic uncertainties.

The expected shape of the $b\bar{b}$ rapidity correlation is determined by the underlying QCD production mechanism and the parton distribution functions (PDFs) of the proton. At leading order in perturbative QCD, $b\bar{b}$ pairs are produced through $q\bar{q}$ annihilation and gluon fusion (Fig. 1). The annihilation process leads to a rapidity correlation $d\sigma/dt \sim(\cosh\Delta y)^{-2}$ at large $\Delta y=y_b-y_{\bar{b}}$, while the gluon fusion process gives rise to a less-pronounced rapidity correlation $d\sigma/dt\sim(\cosh\Delta y)^{-1}$ [15]. For either process, the partonic cross section is suppressed as the rapidity difference increases and it is expected that a $b\bar{b}$ pair will be found closely separated in rapidity. In Fig. 2, we show representative Feynman diagrams for the three general next-to-leading order (NLO) $b\bar{b}$ production processes: (a) direct, (b) flavor excitation, and (c) gluon splitting. The first two processes lead to a broadening of the Δy distribution while the gluon splitting process leads to an enhancement for $\Delta y\approx 0$. For this analysis, we require a minimum azimuthal opening angle between the *b* and $\bar{b}$ decay products that suppresses the contribution from gluon splitting. The shape of the NLO Δy distribution is therefore expected to be similar to the leading-order dependence described above. This is in direct contrast to measurements of the differential cross section $d\sigma/d(\Delta\phi)$, which are directly sensitive to the relative contributions of the different NLO production processes due to the trivial leading order $\Delta\phi$ dependence.

In general, the center-of-mass of the scattering partons is boosted in the laboratory frame, and consequently, the observed rapidity correlation will depend on the PDFs of the proton. In particular, production of high-momentum *b* hadrons in the forward region is sensitive to the PDFs at large momentum fraction *x*. Since the gluon fusion process dominates the $b\bar{b}$ production cross section at the Tevatron, the shape of the *b*-quark rapidity distribution at large *y* is sensitive to the shape of the gluon distribution $G(x,Q^2)$ at large *x*. An accurate measurement of forward *b* production could provide an important constraint on the gluon distribution at high *x*, a region where direct experimental information is still rather limited [16].

In this paper we present the first direct measurement of $b\bar{b}$ rapidity correlations in $p\bar{p}$ collisions at $\sqrt{s}=1.8$ TeV. Specifically, we measure the ratio $R\equiv\sigma(2.0<|y_{b_1}|<2.6)/\sigma(|y_{b_1}|<0.6)$, given that the second *b* quark is observed in the central rapidity range $|y_{b_2}|<1.5$, and both quarks have transverse momentum $p_T>25$ GeV/c and are separated by an azimuthal opening angle $\Delta\phi$ exceeding 60°. We use the presence of a forward or central muon as the initial signature of *b* decay and identify the second quark as

a central recoil jet associated with a decay vertex (secondary vertex) displaced from the $p\bar{p}$ interaction vertex (primary vertex). The fraction of events due to $b\bar{b}$ production is determined by simultaneously fitting the muon momentum relative to a nearby jet, p_T^{rel}, and the transverse decay length of the secondary vertex in the recoil jet. The data used for this analysis correspond to 77 pb^{-1} of $p\bar{p}$ collisions collected by CDF between January 1994 and July 1995 (Run 1B).

The remainder of this paper is organized as follows. Section II describes the detector and trigger systems used to identify muons, jets, and displaced vertices. Section III describes the selection criteria used to isolate a sample of events consistent with $b\bar{b}$ production, and Sec. IV describes the efficiency and acceptance for detecting $b\bar{b}$ events passing the analysis cuts. In Sec. V, we describe the fitting procedure used to determine the $b\bar{b}$ purity in our data, and several consistency checks on the fit results. The cross section ratio is presented and analyzed in Sec. VI, and concluding remarks are given in Sec. VII.

II. DETECTOR

The CDF detector has been described in detail elsewhere [17]. We use a cylindrical coordinate system (r,ϕ,z) with the z axis aligned along the proton beam direction. Polar angle θ and azimuthal angle ϕ are measured from the z and x axes, respectively, and transverse quantities correspond to projections in the r-ϕ plane. For this analysis we use pseudorapidity $\eta \equiv -\ln[\tan(\theta/2)]$ for muon measurements and detector pseudorapidity η_D for jet measurements, where the former is calculated with respect to the reconstructed primary vertex and the latter is defined with respect to $z=0$. For consistency with the cross section definition, we use y for b quarks generated in ISAJET and let the Monte Carlo Program relate the measured η rates to the physical y rates. In this section we describe the tracking, muon, calorimeter, and trigger subsystems used to identify muons, jets, and displaced vertices from b decay.

A. Tracking system

Charged particle trajectories are reconstructed using the CDF central tracking system, which consists of three complementary detectors immersed in a 1.4 T solenoidal magnetic field aligned along $\hat{z}$. Closest to the beam, a silicon microvertex detector (SVX) [18,19] provides precision spatial resolution in the transverse plane. The device consists of four concentric layers of silicon strip detectors grouped into two modules extending 25.5 cm in each direction along the beam line. The inner and outer detector layers are at radii of 2.9 and 7.9 cm, respectively. The impact parameter resolution is measured to be $\sim(13+40/p_T)\ \mu$m for isolated tracks, where p_T is the transverse momentum in GeV/c.

Just outside the SVX, a set of vertex time projection chambers (VTX) measure charged particle trajectories in the r-z plane to a radius of 22 cm and over the pseudorapidity range $|\eta|<3.25$. During Run 1B, $p\bar{p}$ collisions were distributed along z according to a Gaussian distribution with $\bar{z}=0$, and $\sigma_z \approx 30$ cm. Information from the VTX is used to measure the z position of the $p\bar{p}$ interaction vertex with an accuracy of ~ 1 mm.

The outermost tracking detector, the central tracking chamber (CTC) [20], provides full three-dimensional track reconstruction to a radius of 132 cm. The CTC is a cylindrical drift chamber consisting of 84 layers of sense wires grouped into alternating axial and $\pm 3°$ stereo superlayers. Fast timing information from the CTC was used to identify events containing a high-p_T track early in the trigger process, while tracks reconstructed offline were used for central-muon momentum measurements, and as seeds for SVX pattern recognition. The momentum resolution of the CDF tracking system is $\delta p_T/p_T = \sqrt{(0.002p_T)^2+(0.0066)^2}$ for CTC tracks, where p_T is in GeV/c. The resolution improves to $\sqrt{(0.0009p_T)^2+(0.0066)^2}$ for tracks using both CTC and SVX information.

B. Muon systems

The CDF muon systems used in this analysis are the central muon (CMU) [21], central muon upgrade (CMP), and forward muon (FMU) [22] detectors. Located just outside the 5 absorption lengths (at normal incidence) of material comprising the central hadron calorimeter, the CMU consists of four layers of drift chambers with sense wires aligned parallel to the beam direction. The CMP is located behind an additional 60 cm of steel absorber and consists of four more layers of axially-aligned drift chambers. Requiring CMP hits substantially reduces the background from hadrons escaping the central calorimeter. CMU and CMP segments are defined as sets of two or more hits in each detector, and a central-muon candidate is identified by matching a CTC track with both a CMU and CMP segment in ϕ and z. Charge division in the CMU is used to measure the z position of the muon segment. The combined CMU-CMP system covers 53% of the solid angle for $|\eta|<0.6$. Identified central-muon candidates are referred to as CMUP muons.

The FMU is a forward/backward magnetic spectrometer consisting of three planes of drift chambers sandwiching two 1 m-thick iron toroids. The detector planes (front, middle, rear) are located at $|z| \approx 10, 11.5, 13$ m and are divided into 24 chambers, each covering 15° in ϕ and staggered in z to allow for overlap at the edges. The chambers consist of two planes of half-cell staggered drift cells separated by a copper cathode plane, with each cell containing a sense wire strung along a chord in azimuth. Cell size increases with increasing r and z to provide a projective tower geometry for triggering. The cathode plane is divided into 15 ''pads,'' each covering 5° in ϕ and 3° in θ, which provide the ϕ position of reconstructed FMU tracks. In addition, two planes of scintillator with 5° azimuthal segmentation cover the front and rear detector planes. A forward muon candidate consists of 6 drift-cell hits projecting back to the interaction point, 3 cathode-pad hits aligned in η and ϕ, and 2 scintillator hits matching the pad hits in ϕ.

The FMU toroids are instrumented with four 28-turn copper coils each carrying a current of 600 A, generating an

azimuthal magnetic field varying from 1.96 T at the inner radius (50 cm) to 1.58 T at the outer radius (380 cm). Tracks are reconstructed from drift-cell hits using an iterative fitting procedure which takes into account multiple Coulomb scattering and energy loss in the toroids. The track momentum is determined from the fitted curvature in the magnetic field region, and the resolution is $\delta p_T/p_T \approx 15\%$. The FMU system covers the full solid angle for the pseudorapidity range $1.9<|\eta|<3.7$.

C. Calorimeter systems and jet identification

The CDF calorimeter system [23] comprises central ($|\eta|<1.1$), plug ($1.1<|\eta|<2.4$), and forward ($2.4<|\eta|<4.2$) regions divided into electromagnetic (lead absorber) and hadronic (iron absorber) compartments. Each calorimeter is segmented in η and ϕ to provide a projective tower geometry. The central calorimeters use scintillator as the active medium and have a tower size of $\Delta\eta\times\Delta\phi=0.1\times 15°$. The plug and forward calorimeters use gas as the active medium and have a tower size of $\Delta\eta\times\Delta\phi=0.1\times 5°$.

Jets are identified as clusters of energy deposition in the calorimeters using a fixed-cone clustering algorithm [24]. We use a cone size of $R=\sqrt{\Delta\eta^2+\Delta\phi^2}=0.7$ for this analysis. The total jet energy, defined as the scalar sum of measured energies in the towers assigned to the jet, is corrected for detector effects (including η_D-dependent corrections) and underlying event energy using the standard CDF corrections [25]. The jet momentum vector is calculated assuming the energy in each tower was deposited by a single massless particle originating from the primary vertex. The direction of this vector defines the jet axis that we use to calculate $p_T^{\rm rel}$ for the muons in this analysis. The approximate jet energy resolution is $(0.1p_T+1.0)$ GeV, where p_T is in GeV/c [26].

D. Trigger system

The CDF trigger system [27] is divided into first and second level hardware triggers and a third level software trigger based on a version of the offline reconstruction package optimized for execution speed. This analysis uses data acquired with the inclusive central muon and forward muon+jet triggers.

1. Central muon trigger

The level 1 high-p_T central-muon trigger required matching CMU and CMP segments corresponding to a nominal p_T threshold of 6 GeV/c. A coarse p_T measurement is achieved by exploiting the fact that low momentum tracks emerge from the magnetic field at an angle with respect to the radial direction, producing different arrival times on the radially-aligned wires of the CMU detector. The level 2 trigger required a match within 5° in ϕ between the CMU segment and a two-dimensional (r-ϕ) CTC track found by the central fast tracker (CFT) [28]. The CFT is a dedicated hardware track processor programmed to identify predetermined hit patterns corresponding to p_T thresholds from 2.2 to 27 GeV/c. The matched CFT track was required to have $p_T>7.5$ GeV/c. This trigger had its rate reduced (prescaled) by accepting a fraction of the events based on the instantaneous luminosity. The level 3 trigger performed full three-dimensional tracking and required CMU and CMP segments matched to a CTC track with $p_T>6$ GeV/c. Approximately 7 million events were collected with the central muon trigger.

2. Forward muon+jet trigger

The FMU level 1 trigger employed pattern recognition units to search for sets of drift-cell, pad, and scintillator hits consistent with the expected signature of a high-p_T muon originating from the interaction point. Track candidates were identified as sets of 6 drift-cell hits satisfying a tight trigger road in η, while sets of 3 pad hits aligned within 5° in ϕ and 3° in θ were matched to front-rear scintillator pairs within 5° in ϕ. The trigger required the presence of a track candidate and pad-scintillator match in the same ϕ octant, and was approximately 50% efficient at 7.5 GeV/c. The maximum rate for this trigger was limited to 0.6 Hz during Run 1B.

No additional requirements were applied at level 2. At level 3, the FMU track reconstruction code was executed, and the trigger required at least one track with $p_T>4$ GeV/c. Although the FMU was instrumented to $|\eta|=3.7$, large backgrounds near the Tevatron beam pipe restricted the active trigger coverage to $1.9<|\eta|<2.7$. Further background suppression of sources not associated with the $p\bar{p}$ collision was accomplished by requiring the total number of sense wire hits in the active region of the trigger octant to be less than 31, corresponding to a maximum occupancy of 13%. Finally, real muon backgrounds from the decay of vector bosons and light mesons were suppressed relative to heavy-quark decays by requiring at least one jet in the event with uncorrected $E_T>20$ GeV. Approximately 150,000 events were collected with the forward muon+jet trigger.

III. EVENT SELECTION

The selection criteria applied in this analysis are designed to detect both the b and $\bar{b}$ by identifying the semileptonic decay of one b hadron to a muon and jet, and the inclusive decay of the second b hadron using a secondary-vertex tagging algorithm. The muon and the jet containing it are collectively referred to as the μ tag, while the jet tagged by the secondary vertexing algorithm is referred to as the SVX tag. Events are classified as forward or central depending on whether the muon is FMU or CMUP, respectively. This section describes the cuts used to define the forward and central samples.

Beginning with the two muon-triggered data samples, a three-dimensional primary vertex location was determined event-by-event by combining the VTX z position, the average Tevatron beam line position, and SVX tracks, where tracks with large impact parameters with respect to the fitted vertex were removed by an iterative procedure. The resulting vertex was required to have $|z|<30$ cm to keep events in the region of good SVX acceptance. Jets were then reclustered with respect to this vertex and all FMU tracks were refit using the new vertex as a constraint.

A. μ tag requirements

Forward and central muon candidates are required to pass their respective trigger criteria. Poorly measured forward muons are rejected by requiring that the track-fit confidence level exceed 1%. Central muons must satisfy tight segment-track matching requirements. The position of the CTC track extrapolated to the muon chambers must match within 3σ in ϕ and $\sqrt{12}\sigma$ in z, where σ is the rms spread due to multiple Coulomb scattering taking into account energy loss in the calorimeters. The track is also required to point to the primary vertex within 5 cm in z. We require a minimum muon p_T of 6 GeV/c for both samples. Forward muons are restricted to the pseudorapidity range $2.0<|\eta|<2.6$ to match the extent of the CMU coverage ($|\eta|<0.6$). In each event, the highest-p_T muon passing all of the above cuts is used. The μ jet is then identified as the jet with the minimum separation in η-ϕ space from the muon. This separation is required to be <0.7 and the μ jet must satisfy $E_T>15$ GeV. Forward and central μ jets are restricted to the regions $1.9<|\eta_D|<2.7$ and $|\eta_D|<0.7$, respectively.

B. SVX tag requirements

The SVX tag is identified as a central jet ($|\eta_D|<1.5$) with corrected $E_T>26$ GeV and tagged by the CDF secondary-vertexing algorithm [29]. The SVX-tag jet must be distinct from the μ jet defined above. The algorithm begins by assigning SVX tracks to the nearest jet within a cone of 0.7, where track pairs consistent with K_S or Λ decays are removed from the list. The strategy is to make a first attempt at finding a vertex using loose track cuts but requiring $\geqslant 3$ tracks in the tag. The track quality cuts include $p_T>0.5$ GeV/c and impact parameter significance $d_0/\sigma_{d_0}>2.5$, where d_0 is the distance between the track and primary vertex in the transverse plane at closest approach to the vertex. In addition, the highest p_T track must have $p_T>2.0$ GeV/c. If this attempt fails, tighter track cuts ($p_T>1.0$ GeV/c, $d_0/\sigma_{d_0}>3.0$) are applied and a vertex with $\geqslant 2$ tracks is required. If a vertex is found, the signed transverse decay length L_{xy} is defined as the projection of the two-dimensional vector from the primary to the secondary vertex onto the jet axis in the transverse plane. We require $|L_{xy}|/\sigma \geqslant 2.0$, where σ is the total error on L_{xy}, including the contribution from the primary-vertex fit. The efficiency for tagging b jets is determined from Monte Carlo to be 45%, and is approximately equal in the forward and central samples. There are 391 forward and 7737 central events containing both a μ-jet candidate and SVX-tag candidate.

C. Opening angle requirement

There is one final cut applied to both samples. Once the SVX tag is identified, we require $\Delta\phi(\text{tags})>60°$, where $\Delta\phi$ is the azimuthal opening angle between the SVX-tag jet axis and the vector sum of the muon and μ-jet momenta. The motivation for this cut is illustrated in Fig. 3, where we show the observed $\Delta\phi(\text{tags})$ distributions in the forward and central data samples, compared with the corresponding $b\bar{b}$ $\Delta\phi$ distributions from the NLO QCD calculation of Mangano, Nason, and Ridolfi (MNR) [10]. The gluon splitting process produces $b\bar{b}$ pairs that are closely separated in η-ϕ space, leading to an enhancement in the cross section for $\Delta\phi\approx 0$. By definition, the forward-central topology requires a minimum $b\bar{b}$ opening angle and no such enhancement is observed, either in the QCD prediction or in the data. For the central-central topology, where the b and $\bar{b}$ can occupy overlapping regions in η-ϕ space, QCD predicts a significant gluon splitting contribution. However, the event yield in the central sample is observed to decrease for $\Delta\phi<60°$ due to the requirement that the b and $\bar{b}$ decay products are reconstructed as separate jets. The presence of the gluon splitting process in only the central sample leads to a model dependence in the acceptance calculation that does not cancel in the cross section ratio. By requiring $\Delta\phi(\text{tags})>60°$, we explicitly remove the contribution from gluon splitting, which allows us to ignore this process in the acceptance calculation. Our measurement is therefore insensitive to gluon splitting production. There are 382 (7544) forward (central) events remaining after the $\Delta\phi$ cut.

IV. EFFICIENCY AND ACCEPTANCE

In this section we describe the efficiency and acceptance for detecting forward and central $b\bar{b}$ events satisfying the triggers and offline cuts applied in this analysis.

A. Forward muon efficiency

The efficiency of the 0.6 Hz rate limit on the FMU level 1 trigger was calculated to be 39.6% and is included in the acceptance calculation. The remaining trigger requirements are decomposed into kinematic and detector efficiencies. The kinematic efficiency, included in the acceptance calculation, is defined as the probability that a muon of a given p_T will produce a set of 6 drift-cell hits satisfying the trigger pattern for a detector with 100% detector efficiency. The detector efficiency is defined as the product of drift cell, cathode pad, scintillator, and trigger electronics efficiencies and is measured in a sample of $Z^0\rightarrow\mu^+\mu^-$ decays, where the trigger muon is CMUP and the second muon is FMU. Figure 4 shows the dimuon mass distribution for muon pairs with opposite charge. The fraction of same-charge events in the total sample is 3.5%, indicating a correspondingly small fake background in the opposite-charge sample. The combined detector efficiency is $71.4\pm 1.6\%$.

The level 3 occupancy cut required <31 drift-cell hits in the trigger octant. The efficiency of this cut was measured in a sample of FMU level 1 triggers rejected by the 0.6 Hz rate limit, but subsequently accepted through an independent trigger path. Figure 5 shows the efficiency as a function of instantaneous luminosity. We perform a linear fit constraining $\epsilon(\mathcal{L}=0)=1.0$ and convolute the resulting functional form with the luminosity distribution observed in events passing the FMU level 1 trigger. The resulting efficiency is $88.5\pm 0.4\pm 0.5\%$, where the first uncertainty is statistical and the second is due to uncertainty on the fitted slope.

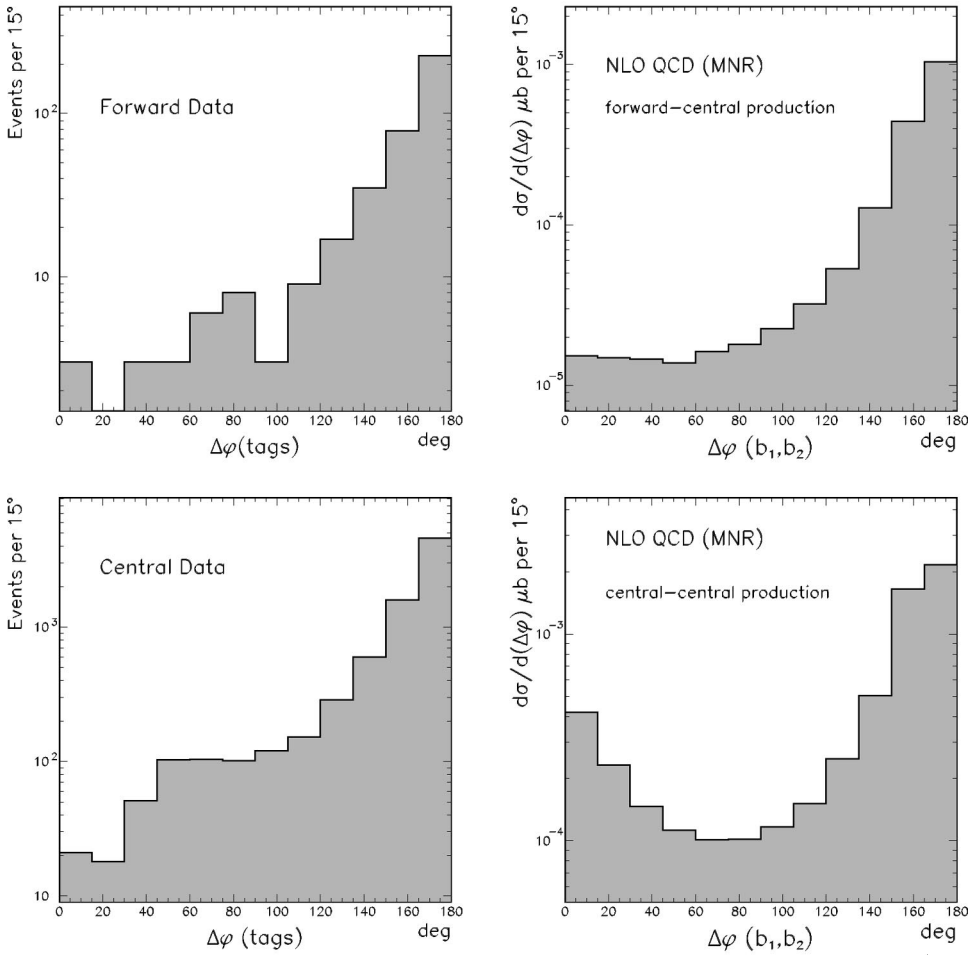

FIG. 3. The observed azimuthal opening angle between the μ tag and SVX tag in forward (top left) and central (bottom left) data events compared to the NLO QCD $\Delta\phi(b_1,b_2)$ distribution for the forward-central (top right) and central-central (bottom right) topologies.

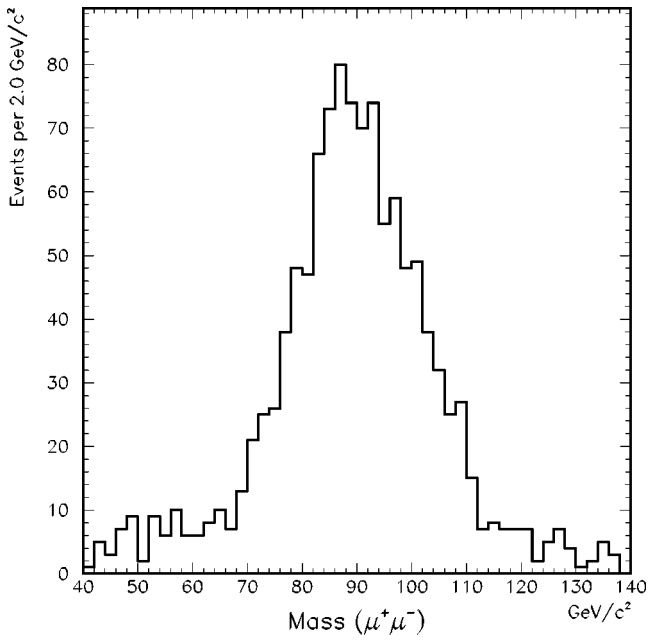

FIG. 4. Invariant mass distribution for the opposite charge FMU-CMU muon pairs used to measure the FMU detector efficiency.

The efficiency of the level 3 jet requirement was measured in a sample of events passing the inclusive FMU trigger and containing a jet with corrected $E_T > 26$ GeV and $|\eta_D| < 1.5$. The inclusive trigger required a muon passing the same cuts as the FMU+jet trigger, but with a higher p_T threshold (15 GeV/c). The efficiency, calculated as the fraction of events in the sample that pass the FMU+jet trigger, was found to be $98.6 \pm 0.3\%$.

The efficiency of the confidence-level cut on the FMU track fit was measured in the same CMUP-FMU Z^0 sample used to measure the level 1 detector efficiency. We find the efficiency for requiring a confidence level exceeding 1% to be $92.0 \pm 1.0\%$. This result is consistent with the efficiency determined from a detailed Monte Carlo simulation of the FMU detector as well as the efficiency measured directly in the forward muon+jet trigger sample.

B. Central muon efficiency

The level 1 CMU and CMP segment-finding efficiencies were measured in a sample of $Z^0 \rightarrow \mu^+\mu^-$ events by comparing the number of muon segments with 3 drift chamber hits to the number with 4 hits, from which the single hit efficiency was derived. The combined efficiency for requiring 2 or more hits in both the CMU and CMP detectors is $98.1 \pm 0.3\%$. The efficiency of offline matching requirements between the CTC track and muon segments was measured in a sample of $J/\psi \rightarrow \mu^+\mu^-$ events to be $98.5 \pm 0.2\%$. The-

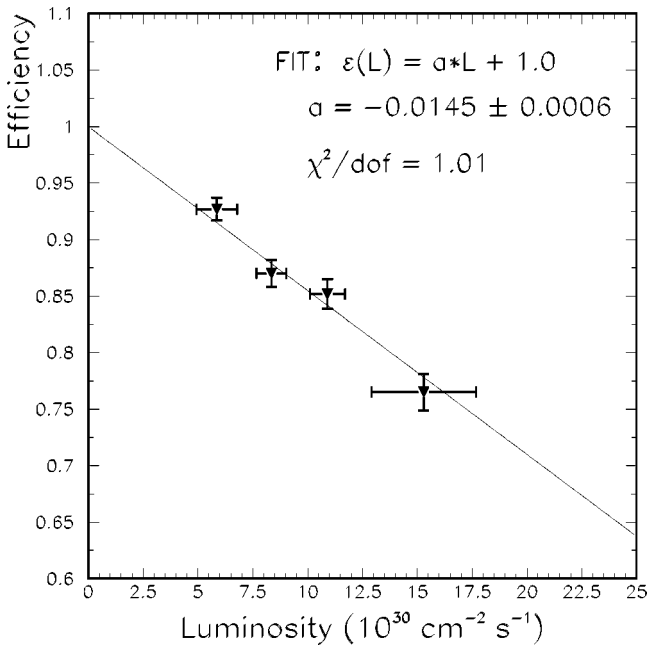

FIG. 5. Efficiency of the FMU level 3 occupancy cut as a function of instantaneous luminosity. Data points are plotted at the mean of four luminosity bins: 1.0–7.2, 7.2–9.6, 9.6–12.4, >12.4. Horizontal error bars correspond to the variance in each bin. The solid line is a linear fit to the data with the constraint $\epsilon(\mathcal{L}=0)=1.0$.

segment-finding and track-matching efficiencies are combined into a CMUP identification efficiency of $96.6\pm0.4\%$.

The central muon trigger efficiencies were measured in independently triggered samples of J/ψ and Z^0 events. The level 3 plateau efficiency was measured to be $98.5\pm1.0\%$, while the level 1 and level 2 triggers are parameterized as a function of p_T and included in the trigger simulation as part of the acceptance calculation. The efficiency of the level 2 prescale was calculated to be 55.9% and is also included in the central muon trigger simulation.

The track-finding efficiency in the CTC was studied by embedding Monte Carlo tracks into real J/ψ events [30,31]. For $p_T>1$ GeV/c the tracking efficiency is constant and measured to be $96.2\pm0.9\%$, where the uncertainty is statistical only.

C. Acceptance

The acceptance calculation includes the muon geometric and kinematic cuts, trigger efficiency, jet identification, and *b*-tagging requirements in one Monte Carlo program. The acceptance is defined as the number of events satisfying all cuts divided by the number of generated events satisfying the cross section cuts (defined below).

The Monte Carlo program uses ISAJET [32] version 7.06 to generate $b\bar{b}$ events with Martin-Roberts-Stirling Set A′ (MRSA′) [33] PDFs, Peterson fragmentation with $\epsilon=0.006$ [34,35], and a *b*-quark mass of 4.75 GeV/c^2. The event *z*-vertex position is chosen randomly from a Gaussian distribution with $\bar{z}=0$ and $\sigma_z=29$ cm. Since the efficiency of the *z*-vertex cut cancels in the cross section ratio, events are only generated in the range $|z|<30$ cm. ISAJET treats the direct, flavor excitation, and gluon splitting production processes as incoherent and any difference in acceptance will lead to a dependence on the relative cross sections. Fortunately, we find that the acceptance for the direct and flavor excitation processes are equal within Monte Carlo statistics and the gluon-splitting process is negligible after the $\Delta\phi>60°$ requirement. The acceptance calculation is therefore defined with respect to direct production only. We have confirmed that the ISAJET p_T and y distributions for the b and $\bar{b}$ agree with the full NLO calculation.

The CLEO Monte Carlo program, QQ [36], is used to model the *b*-hadron decays. The full decay table is used to include the effects of sequential decays ($b\to c\to\mu$). The muon branching fraction, defined as the fraction of all $b\bar{b}$ events that produce a muon from heavy-quark decay, cancels in the cross section ratio. The branching fraction is therefore removed from the acceptance calculation by redecaying events until at least one *b* quark produces a muon in its decay chain.

Generated events are simulated using the full CDF simulation package. The central muon trigger is simulated by applying the measured level 1 and level 2 trigger efficiency parameterizations, including the effect of the prescale on the 7.5 GeV/c level 2 trigger. The forward muon level 1 trigger is simulated by requiring that the drift-cell hits used in reconstructing the track satisfy the trigger pattern. The FMU detector simulation includes extra hits from delta rays and muon bremsstrahlung distributed according to the results of a detailed model of multiple scattering and energy loss in the calorimeters and toroids. Events satisfying the trigger are treated like real data, requiring both a μ tag and SVX tag passing the offline cuts.

The acceptance is calculated separately for the forward and central topologies using two independently generated Monte Carlo samples. Forward events are generated with both quarks having $p_T>15$ GeV/c, one quark in the rapidity range $1.65<|y|<3.0$, and the second quark with $|y|<1.65$. Central events are generated with the same p_T threshold and a rapidity requirement of $|y|<1.65$ for both quarks. These cuts were designed to minimize any bias by extending into the regions of zero acceptance. We use the kinematic relationship between the μ-tag candidate, the SVX-tag candidate, and the $b\bar{b}$ quark spectra to obtain the $b\bar{b}$ rapidity correlation over a p_T range from a threshold $p_T^{\min}$ to infinity. We use $p_T^{\min}=25$ GeV/c, where the threshold was chosen so that 90% of the events satisfying all cuts originate from *b* quarks with $p_T>p_T^{\min}$. The acceptance for the forward sample, including the efficiency (39.6%) of the level 1 rate limit, is $(7.73\pm0.09)\times10^{-3}$. The corresponding acceptance for the central sample is $(2.54\pm0.06)\times10^{-2}$. The uncertainty in both cases is statistical only. The smaller acceptance in the forward sample is due almost entirely to the lower kinematic acceptance of the toroids relative to the central detectors and the steeper $d\sigma/dp_T$ production spectrum in forward $b\bar{b}$ events.

The total efficiency for detecting a forward or central topology combines the efficiency measurements and acceptance calculation described above. Tables I and II summarize

TABLE I. Summary of the total efficiency for the forward sample. Errors are statistical only.

Cut	Efficiency
Acceptance	$(7.73\pm0.09)\times10^{-3}$
Level 1	0.714 ± 0.016
Splash Cut	0.885 ± 0.004
L3 Jet Cut	0.986 ± 0.003
C.L. (χ^2)	0.920 ± 0.010
Total forward ϵ	$(4.43\pm0.12)\times10^{-3}$

the results for the forward and central samples, respectively. The relative efficiency (central/forward) is 5.24 ± 0.21.

V. FITTING PROCEDURE AND RESULTS

There are several physics processes besides $b\bar{b}$ production that contribute to the data samples described in Sec. III. These include $c\bar{c}$ production, heavy-quark production in association with a high-p_T gluon or light-quark jet that fakes a μ tag or SVX tag, generic dijet events producing two fake tags, and $Z^0\rightarrow b\bar{b}$ decay. Four-heavy-quark production ($b\bar{b}b\bar{b}$,$b\bar{b}c\bar{c}$,$c\bar{c}c\bar{c}$) has been calculated to leading order [37] and is estimated to be negligible. We determine the fraction of events in each sample consisting of two real b tags by simultaneously fitting the p_T of the muon relative to the μ-jet direction, and the transverse proper decay length of the SVX tag. The number of $b\bar{b}$ events due to Z^0 decay is then estimated using the CDF measured cross section and a Monte Carlo acceptance calculation. The remainder of this section describes the templates used in the fit, the fit results and Z^0 subtraction, and several consistency checks.

A. Templates

1. Pseudo-ct

The transverse proper decay length of the SVX-tag secondary vertex is estimated with the following equation,

$$\text{pseudo-}ct = L_{xy}\frac{M}{p_T}, \tag{1}$$

where the mass M and p_T are calculated with the assumption that the tracks used in the tag are pions, and ''pseudo'' refers to the fact that we do not fully reconstruct the b hadron. In Fig. 6, we show the pseudo-ct distributions used as templates for bottom, charm, and fake SVX tags, where ''fake'' tags are defined as tagged jets which do not contain a heavy quark. The shape of the b quark distribution is obtained from the Monte Carlo samples used in the acceptance calculation. A similar Monte Carlo simulation is used to generate forward and central samples of $c\bar{c}$ events passing the same requirements as the $b\bar{b}$ samples. The shapes of the bottom and charm pseudo-ct distributions in the forward sample are similar to the corresponding distributions in the central sample.

TABLE II. Summary of the total efficiency for the central sample. Errors are statistical only.

Cut	Efficiency
Acceptance	$(2.54\pm0.06)\times10^{-2}$
Muon ID	0.966 ± 0.004
Level 3	0.985 ± 0.010
Tracking	0.962 ± 0.009
Total Central ϵ	$(2.32\pm0.07)\times10^{-2}$

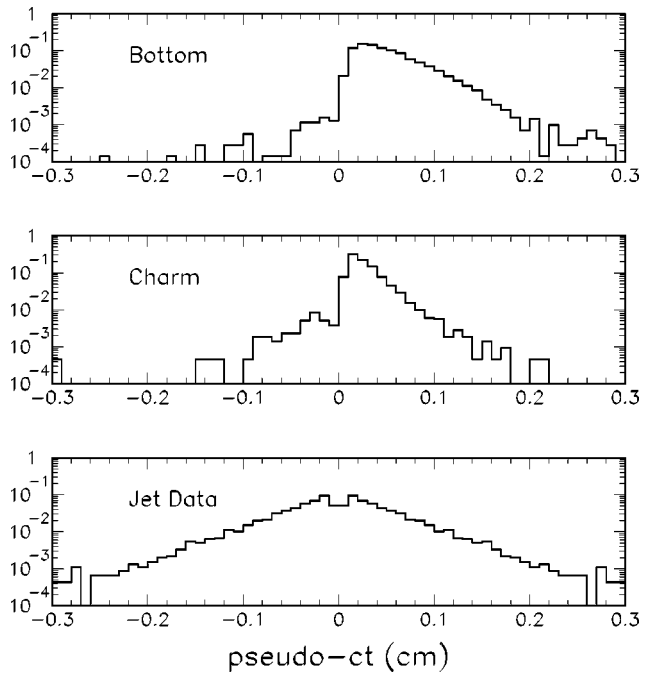

FIG. 6. Pseudo-ct distributions for the SVX tag in bottom and charm Monte Carlo samples, and for the symmetrized negative tags in jet data. The jet data shape is used as the fake-tag background template.

The fake SVX-tag distribution is constructed in the following way. First, we note that fake tags from random track combinations are due to track reconstruction errors, leading to non-Gaussian tails in the SVX resolution function, and are symmetric with respect to $ct=0$ [29]. Second, based on the bottom and charm Monte Carlo distributions in Fig. 6, the fraction of heavy-quark tags with $L_{xy}<0$ is small ($\sim1\%$). We therefore assume that the negative tags in a sample of inclusive jet events will be dominated by fake tags and derive the fake SVX-tag pseudo-ct template by symmetrizing the distribution of negative tags with respect to $ct=0$. The jet sample was obtained from events collected with three inclusive jet triggers with thresholds of 20, 50, and 100 GeV. The resulting fake pseudo-ct template is displayed in the bottom plot of Fig. 6. Although this procedure ignores some sources of real secondary vertices from the decay of long-lived particles, the tagging algorithm explicitly removes the majority of K_S and Λ decays, and the CDF track reconstruction algorithm removes tracks with a large kink that would

arise from π or K decays. Several checks on the pseudo-$c\tau$ fit results are presented in Sec. V C.

2. p_T^{rel}

Due to the large b-quark mass, muons from b decay are, on average, more energetic and have a larger opening angle relative to the remaining decay products than do muons from the decay of hadrons containing charm or lighter quarks. This information is contained in the variable $p_T^{\rm rel}$, defined as the muon p_T relative to the μ-jet axis,

$$p_T^{\rm rel} = p^{\mu} \sin \alpha, \tag{2}$$

where α is the angle between the muon and μ-jet momentum vectors and p^{μ} is the total muon momentum. When determining α, the muon momentum is not included in the μ-jet momentum vector.

The default CDF calorimeter simulation does not accurately reproduce event-by-event fluctuations in the position of the μ-jet energy centroid relative to the muon direction. It was therefore necessary to develop a smearing procedure in order to obtain good agreement between data and Monte Carlo $p_T^{\rm rel}$ distributions. The procedure, a more detailed description of which is presented in Ref. [38], consists of smearing the η and ϕ position of the μ-jet axis according to a Gaussian distribution for some fraction of events. The width of the Gaussian and fraction of events to smear are then tuned to reproduce the observed $\Delta\phi$ and $\Delta\eta$ distributions between the μ-jet axis determined from calorimeter vs. tracking information. This choice of calibration variable is motivated by the good agreement between data and default Monte Carlo $p_T^{\rm rel}$ distributions when the μ-jet axis is obtained from CTC tracks. We apply the same smearing procedure to signal and background Monte Carlo samples in the forward and central regions.

In Fig. 7, we compare the $p_T^{\rm rel}$ distribution obtained from the central $b\bar{b}$ smeared Monte Carlo sample to the subsample of central data events where the μ jet is also tagged by the secondary-vertexing algorithm (double-tagged sample). The b purity in this sample is $>90\%$ and the smeared Monte Carlo sample reproduces the shape of the $p_T^{\rm rel}$ distribution. The shape of the smeared $p_T^{\rm rel}$ distribution in the forward sample is very similar to the central sample (Fig. 8).

Figure 9 shows the $p_T^{\rm rel}$ template distributions for muons from charm and light-meson decays obtained with the same smearing procedure applied to the $b\bar{b}$ Monte Carlo events. Muons from π and K decay are modeled by generating gluon and light-quark events in ISAJET and decaying the produced mesons according to their muon branching fractions and lifetimes. Muons descended from mesons that decay before showering in the calorimeter are simulated and subjected to the same requirements placed on muons from heavy-quark decay. The μ tags from decay-in-flight muons are referred to as ''fake.'' We find that the $p_T^{\rm rel}$ resolution is insufficient to separate fake muons from charm-decay muons. We therefore use the charm distribution to represent both components in the fit. The difference obtained by using the fake template is quoted as a systematic uncertainty.

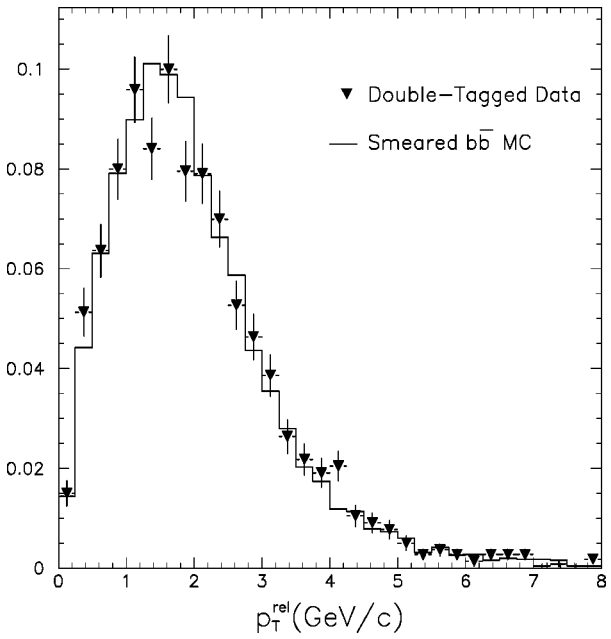

FIG. 7. The $b\bar{b}$ $p_T^{\rm rel}$ distribution from smeared Monte Carlo sample (hist) compared to the subset of central data events where the μ jet also contains a b tag (points).

B. Fit results

With the possibility of having bottom (b), charm (c), and fake (f) tags, there are 9 distinct combinations of SVX and μ tags. However, we do not consider four-heavy-quark produc-

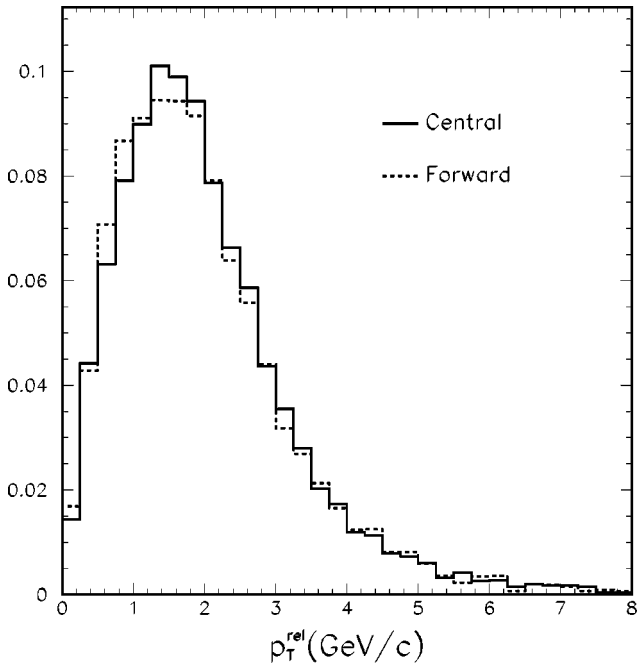

FIG. 8. Comparison of $p_T^{\rm rel}$ distributions in central (solid) and forward (dash) smeared $b\bar{b}$ Monte Carlo samples.

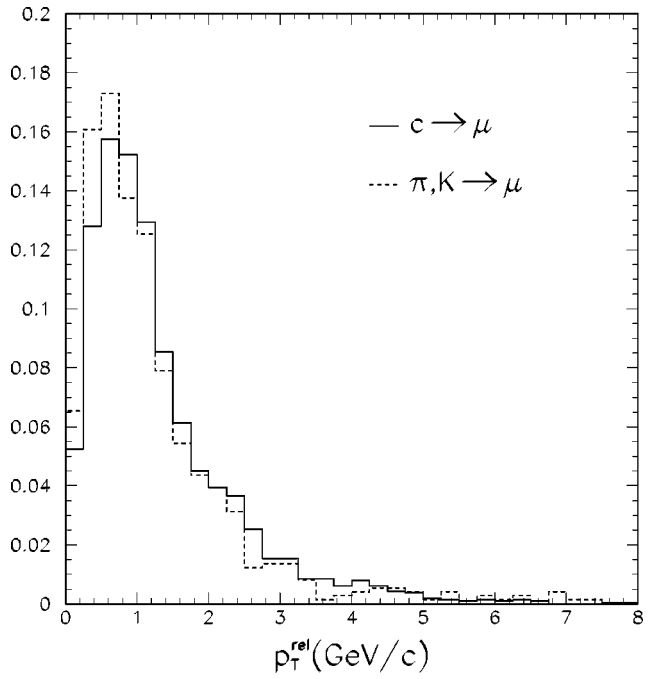

FIG. 9. Distributions of $p_T^{\rm rel}$ for forward muons from the decay of charm (solid), and light mesons (dashed) using smeared Monte Carlo samples.

tion (which excludes the two components with one bottom and one charm tag) and $p_T^{\rm rel}$ does not distinguish charm and fake μ tags, so there are five distinct components in the fit. We label these five components f_{bb}, f_{cc}, f_{bf}, f_{fb}, and f_{fc}, where the first and second indices indicate the source of SVX and μ tags, respectively. The component f_{cc} includes the background combination involving a charm SVX tag and fake μ tag, and f_{fc} includes the background combination with two fake tags. We perform a simultaneous binned maximum likelihood fit using pseudo-ct and $p_T^{\rm rel}$ to determine the relative contribution from these five processes, where the $p_T^{\rm rel}$ fit is separated into events with positive and negative L_{xy}. With the assumption that the negative tags are predominantly fake, this procedure enables the individual determination of the two components with fake SVX tags (f_{fb} and f_{fc}). The only constraint in the fit is that all components must be positive. The fit results are listed in Table III. The χ^2 per degree of freedom is 1.1 and 1.4 for the forward and central fits, respectively. Combining the fitted signal fractions with the total number of events in each dataset, we determine that 311 ± 23 forward and 4655 ± 128 central events are due to $b\bar{b}$ production where both quarks are correctly identified.

TABLE III. Fitted fractions for each source in the forward and central fits. The first and second indices on the component symbols refer to the source of the SVX tag and μ tag, respectively. Fit errors correspond to a change in the log likelihood of 0.5.

Component	Forward Fit	Central Fit
f_{bb}	0.815 ± 0.060	0.617 ± 0.017
f_{cc}	0.083 ± 0.051	0.148 ± 0.014
f_{bf}	$0.000^{+0.059}_{-0.000}$	0.066 ± 0.021
f_{fb}	$0.017^{+0.047}_{-0.017}$	0.070 ± 0.010
f_{fc}	$0.086\pm^{+0.035}_{-0.046}$	0.099 ± 0.010

We show the pseudo-ct and $p_T^{\rm rel}$ fit results for the forward sample in Fig. 10 and for the central sample in Fig. 11. For the $p_T^{\rm rel}$ fits, the main plot shows the distribution in events where the SVX tag has positive L_{xy}, while the inset shows the events with a negative L_{xy} tag. Overall, the fit results are very good. In particular, the fake SVX-tag template obtained from jet data reproduces the shape of the negative pseudo-ct distribution in both samples, and the smeared Monte Carlo $p_T^{\rm rel}$ templates provide a good fit on the μ-tag side.

The expected number of $b\bar{b}$ events due to Z^0 decay is estimated from the $Z^0\to e^+e^-$ cross section measured by CDF [39], the luminosity (77 pb^{-1}), the relative branching fractions [40], and a calculation of the acceptance for detecting $b\bar{b}$ events from Z^0 decay using the same Monte Carlo simulation described in Sec. IV C. We determine that 4.1 ± 0.7 forward, and 203 ± 33 central $b\bar{b}$ events are due to Z^0 decay. These estimated event yields are subtracted from the fitted number of $b\bar{b}$ events in each sample, resulting in a final estimate of 307 ± 23 forward and 4452 ± 132 central $b\bar{b}$ events.

C. Consistency checks

The assumption of a small fraction of negative L_{xy} tags in bottom and charm events has been checked by comparing the $b\bar{b}$ Monte Carlo template to the distribution obtained from the double-tagged central data, Fig. 12. The agreement is very good, giving confidence that the fraction of negative tags in a sample of heavy-quark decays is properly modeled by the Monte Carlo simulation.

The assumed symmetry of the background L_{xy} distribution has been explicitly checked by combining tracks from separate back-to-back jets and constraining them to originate from a common vertex. The resulting pseudo-ct distribution is symmetric with respect to $ct=0$ [29]. As an additional check, in Fig. 13 we compare the fake SVX-tag template derived from jet data with the distribution obtained from a sample of generic Monte Carlo jets tagged by the secondary-vertexing algorithm. The comparison shows some disagreement near $ct=0$. However, replacing the jet-data template with the Monte Carlo template and refitting the data, we find signal fractions of 0.806 ± 0.059 and 0.613 ± 0.017 for the forward and central data, respectively. These results are in excellent agreement with the fits using the jet-data template.

As a final check on the pseudo-ct fit, we use the mass M of the secondary vertex in place of ct and refit the data. The mass and pseudo-ct variables are largely uncorrelated and represent independent estimators of the b purity of the SVX tag. We use the same generic Monte Carlo sample described above to obtain the shape of the fake SVX-tag mass distribution. The bottom and charm templates come from the same samples used to obtain the pseudo-ct templates. We find that the fit cannot independently separate the charm and fake components. We therefore fix the relative contribution

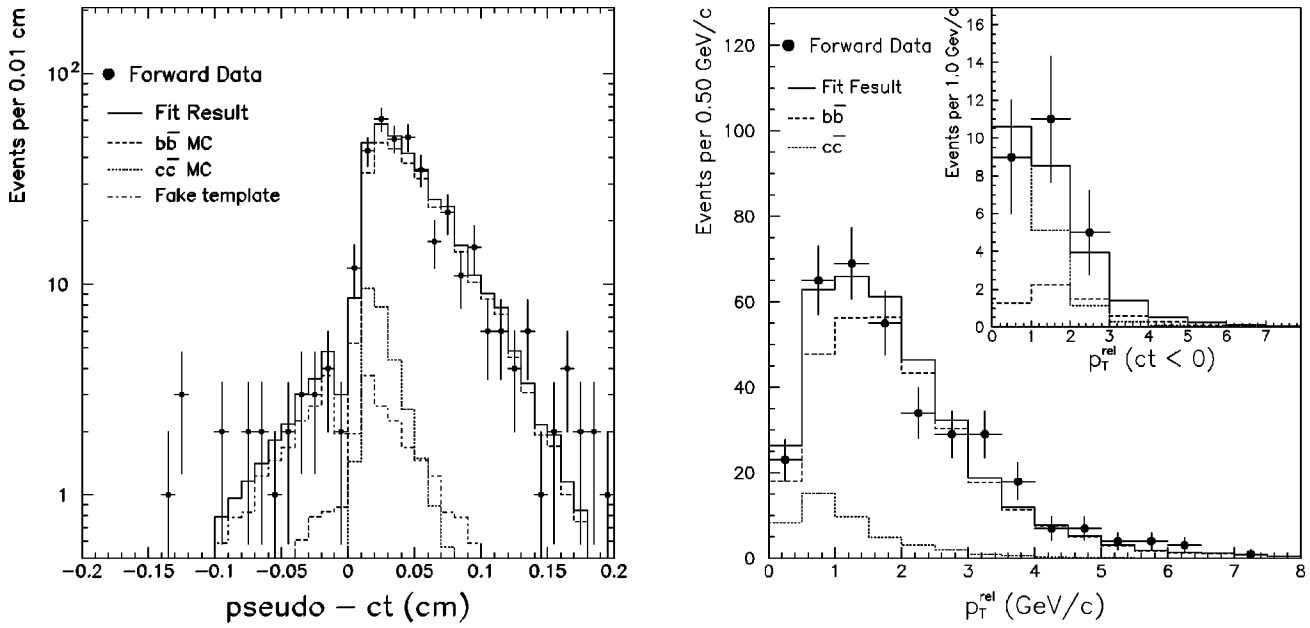

FIG. 10. Forward data fit result for pseudo-ct and $p_T^{\rm rel}$. The main $p_T^{\rm rel}$ plot shows the distribution for events with $ct>0$, while the inset shows the events with $ct<0$.

of charm and fake SVX tags to the result obtained using ct. With this constraint, the fitted $b\bar{b}$ fractions are 0.767 ± 0.051 and 0.616 ± 0.017 for the forward and central fits, respectively, which are consistent with the results using pseudo-ct. The mass fits are displayed in Fig. 14.

Because $p_T^{\rm rel}$ cannot separate muons from charm and light-quark decay, the charm template is used to represent both components in the fits. This choice is somewhat arbitrary, so as a check we substitute the decay-in-flight template and refit the data. We find $b\bar{b}$ fractions of 0.822 ± 0.056 and 0.658 ± 0.015 in the forward and central samples, respectively. The forward result is consistent with the fit using the charm $p_T^{\rm rel}$ template, but there is a systematic shift in the central sample. The relative difference in the ratio of $b\bar{b}$ events from the nominal fit is -5.4%, and we include this as a systematic uncertainty on the cross section ratio.

Finally, as a check on the Monte Carlo smearing procedure we refit the central data using a definition of $p_T^{\rm rel}$ based on tracking, rather than calorimeter, information. The track clustering algorithm is similar to the jet clustering algorithm

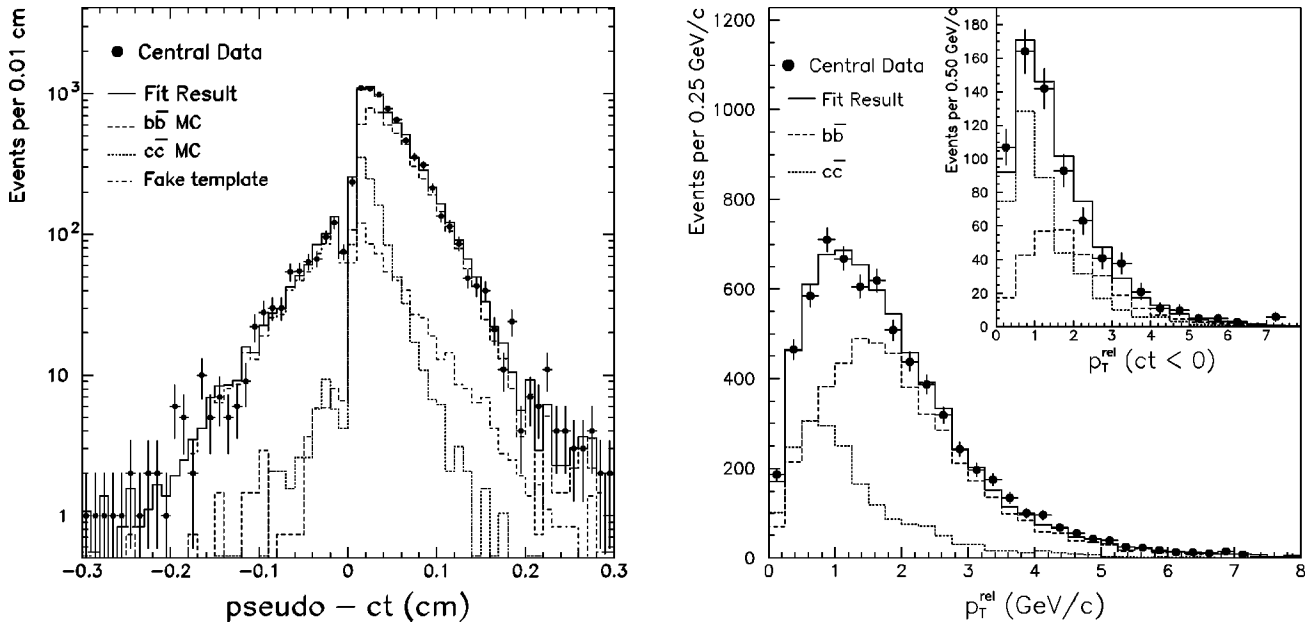

FIG. 11. Central data fit result for pseudo-ct and $p_T^{\rm rel}$. The main $p_T^{\rm rel}$ plot shows the distribution for events with $ct>0$, while the inset shows the events with $ct<0$.

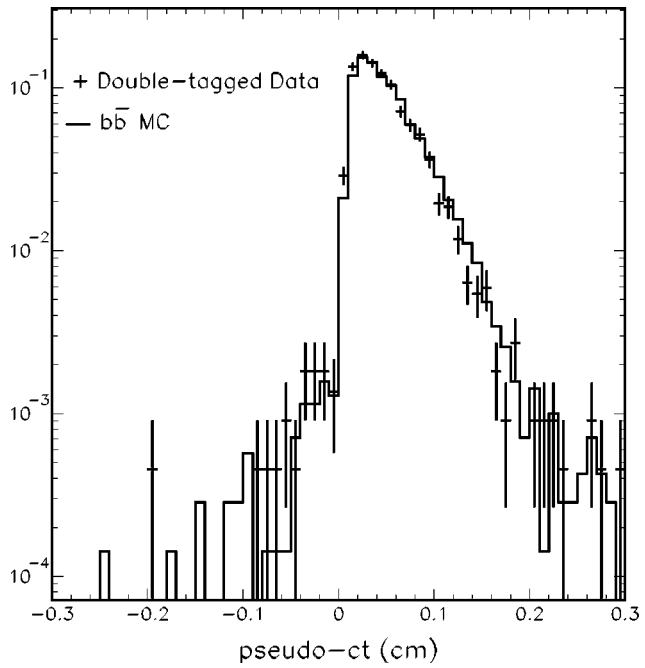

FIG. 12. Comparison between the $b\bar{b}$ pseudo-ct template and the distribution for SVX tags in the subset of central data events where the μ jet also contains a b tag.

with tracks replacing calorimeter towers. The μ jet is unambiguously selected as the jet containing the muon track, and we calculate p_T^{rel} after subtracting the muon momentum vector from the jet. The fit result using this definition of p_T^{rel} is displayed in Fig. 15. The $b\bar{b}$ fraction is 0.641 ± 0.014, which

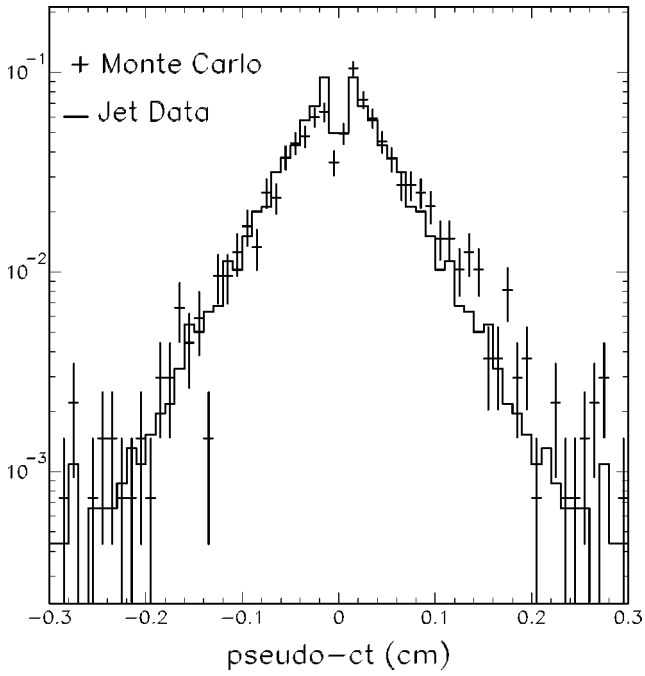

FIG. 13. The pseudo-ct distribution for Monte Carlo gluon and light-quark jets (points) compared to the fake template obtained by symmetrizing the negative pseudo-ct distribution in a sample of inclusive jets (histogram).

is 3.9% higher than the nominal fit. We combine the resulting -3.9% shift in the cross section ratio with the -5.4% systematic uncertainty due to using the decay-in-flight p_T^{rel} template, and assign a total systematic uncertainty of -6.7% on the measured cross section ratio due to uncertainty in the fitted number of $b\bar{b}$ events.

VI. CROSS SECTION RATIO AND COMPARISON WITH QCD

The measured cross section ratio R_{expt} is defined and calculated with the following formula,

$$R_{\mathrm{expt}} = \frac{\sigma(p\bar{p} \to b_1 b_2 X; 2.0 < |y_{b_1}| < 2.6)}{\sigma(p\bar{p} \to b_1 b_2 X; |y_{b_1}| < 0.6)} = \frac{N_{bb}^{\mathrm{f}}}{N_{bb}^{\mathrm{c}}} \frac{\epsilon_{\mathrm{c}}}{\epsilon_{\mathrm{f}}}, \quad (3)$$

where $p_T(b_1)$, $p_T(b_2) > 25$ GeV/c, $|y_{b_2}| < 1.5$, and $\Delta\phi(b_1, b_2) > 60°$ for both cross sections, $N_{bb}^{\mathrm{f(c)}}$ are the number of background subtracted $b\bar{b}$ events in the forward (central) datasets, and $\epsilon_{\mathrm{f(c)}}$ are the total efficiencies. Combining the results of Secs. IV and V, we find $R_{\mathrm{expt}} = 0.361 \pm 0.033$, where the error is statistical only.

A. Systematic uncertainties

The primary motivation for presenting the ratio of forward and central $b\bar{b}$ production, rather than absolute cross sections, is that many of the experimental uncertainties cancel, including the luminosity, the vertex $|z| < 30$ cm requirement, the muon branching fraction, and the secondary-vertexing algorithm b-tagging efficiency. The remaining uncertainties are either reduced or are small to begin with. In this section we describe the estimation of these uncertainties.

The uncertainty on the jet energy scale receives contributions from both the absolute and relative (η_D-dependent) corrections. The main sources of uncertainty on the absolute E_T scale are calorimeter response, fragmentation, and underlying event. The combined systematic uncertainty for these effects is estimated to be 3.6% for corrected jet $E_T = 15$ GeV, decreasing with increasing E_T. Fluctuating the jet E_T cuts $\pm 3.6\%$ changes the event yield by $^{+9.2}_{-10}\%$ and $^{+7.8}_{-7.3}\%$ in the forward and central samples, respectively. The resulting shift in R_{expt} is $^{+1.4}_{-3.2}\%$. Uncertainty on the relative jet energy correction arises from finite statistics in the dijet balancing analysis. Since the correction, and the uncertainty, depends on η_D, the effect of this uncertainty is determined by fluctuating the E_T correction for all jets $\pm 1\sigma(\mathrm{stat})$ and observing the change in event yield. We find the relative change in the number of events to be $^{+1.5}_{-0.5}\%$ in the forward data, and $\pm 0.6\%$ in the central data. The resulting change in R_{expt} is $+1.0\%$.

We use the value 0.006 ± 0.002 for the Peterson fragmentation parameter. Fluctuating ϵ within this uncertainty changes the acceptance by $^{+10}_{-7.2}\%$ and $^{+7.4}_{-7.6}\%$ for the forward and central samples, respectively. The net shift in R_{expt} is -2.7%. Recent experimental studies by the OPAL [41] and ALEPH [42] Collaborations at the CERN e^+e^- collider LEP

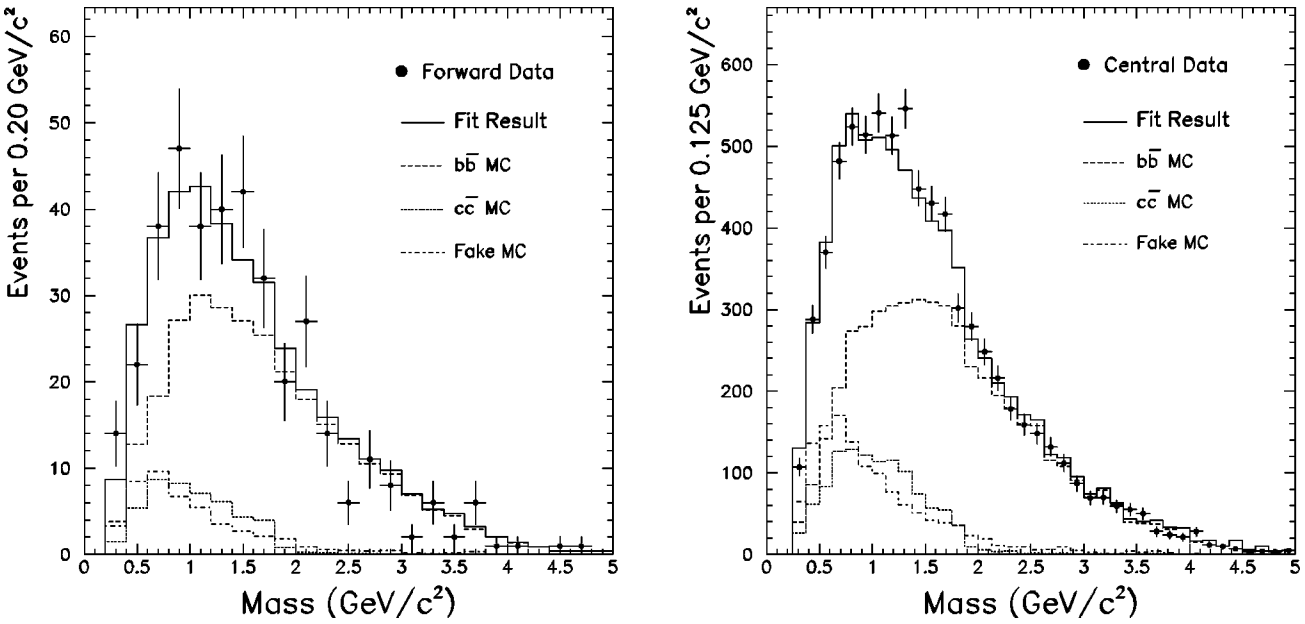

FIG. 14. Fit results for the forward (left) and central (right) data using the mass of the secondary vertex and p_T^{rel}.

favor a value of ϵ closer to 0.003, and a theoretical study [43] using NLO evolution for the perturbative part of the fragmentation function obtained $\epsilon = 0.0015 \pm 0.0002$ using $\Lambda_5 = 200$ MeV. The lower values of ϵ are closely coupled to the modeling of the mix of B hadrons (i.e., the B^{**} fraction) and the amount of gluon radiation; the larger value is appropriate for use with a LO production model with no B^{**} component, such as ISAJET. While studies of b fragmentation have been carried out in the central region at CDF [44], we have not studied the proper epsilon value to use at all rapidities. Nevertheless, in the absence of an experimental determinator of ϵ in the hadron-collider environment, we have calculated the acceptance using the extreme limit $\epsilon \to 0$, with no modification to the LO ISAJET b-quark spectrum. We find individual shifts of $+78\%$ and $+52\%$ for the forward and central acceptance, respectively. This results in a -15% shift in R_{expt}, which can be taken as the maximum range of uncertainty due to fragmentation effects.

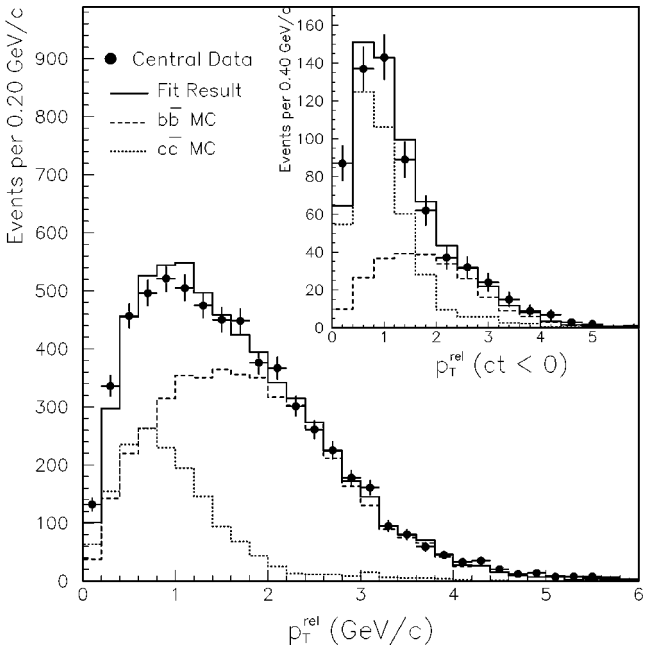

FIG. 15. Result of the central muon data fit using pseudo-ct and track-based p_T^{rel}. Templates are from default Monte Carlo.

The systematic uncertainty on the CTC tracking efficiency takes into account variations with instantaneous luminosity and single-hit efficiency degradation in the inner superlayers over the course of Run 1B. The combined uncertainty from these effects is estimated to be $\pm 3.3\%$.

The uncertainty on the CMUP acceptance calculation was estimated by fluctuating the trigger efficiency parameters within their statistical uncertainties. The resulting systematic uncertainty is $\pm 1.7\%$.

Finally, in Sec. IV A the uncertainty on the FMU level 3 occupancy cut was determined to be $\pm 0.6\%$ by fluctuating the fitted slope within its uncertainty, and the consistency checks in Sec. V C resulted in an estimated uncertainty of -6.7% on R_{expt} due to uncertainty on the fitted number of $b\bar{b}$ events. Table IV summarizes the various sources of systematic uncertainty on R_{expt}. Adding the individual uncertainties in quadrature results in a total systematic uncertainty of $^{+4.1}_{-8.7}\%$. The final value for the measured cross section ratio is $R_{\mathrm{expt}} = 0.361 \pm 0.033\ (\mathrm{stat})^{+0.015}_{-0.031}(\mathrm{syst})$.

B. Comparison with theory

We compare our result to the NLO QCD calculation of Ref. [10] using MRSA′ PDFs, $m_b = 4.75\ \mathrm{GeV}/c^2$, and renormalization/factorization scale $\mu_0 = \sqrt{m_b^2 + \langle p_T^2 \rangle}$, where $\langle p_T^2 \rangle = \frac{1}{2}(p_{T,b}^2 + p_{T,\bar{b}}^2)$. In calculating the theoretical result R_{theor}, the same p_T and rapidity cuts used in the acceptance calculation are applied. We find $R_{\mathrm{theor}} = 0.338^{+0.014}_{-0.097}$, in good

TABLE IV. Summary of systematic uncertainties on the cross section ratio. The total uncertainty is the quadrature sum of the individual uncertainties.

Source	Uncertainty (%)
Jet E_t scale (absolute)	$^{+1.4}_{-3.2}$
Jet E_t scale (relative)	$+1.0$
Fragmentation	-2.7
CTC tracking efficiency	± 3.3
CMUP trigger efficiency	± 1.7
FMU level 3 occupancy cut	± 0.6
Fitting procedure	-6.7
Total Uncertainty	$^{+4.1}_{-8.7}$

agreement with the experimental result. The uncertainty was estimated by changing the scale factor between $2\mu_0$ and $\mu_0/2$.

In Fig. 16, we compare the experimental measurement to the predicted shape of $R=\sigma(y_{b_1})/\sigma(|y_{b_1}|<0.6)$ as a function of y_{b_1}, integrated over rapidity bins of width 0.6 and normalized to the central bin. To illustrate that the b-quark rapidity distribution does not change significantly between LO and NLO, the Born cross section is shown as a dashed line in each bin. Due to the strong rapidity correlation between the b and $\bar{b}$, the predicted $d\sigma/dy_{b_1}$ distribution falls off rapidly once the trigger b is detected outside the rapidity range occupied by the second b ($|y_{b_2}|<1.5$). We find no evidence for anomalous forward B production allowed by

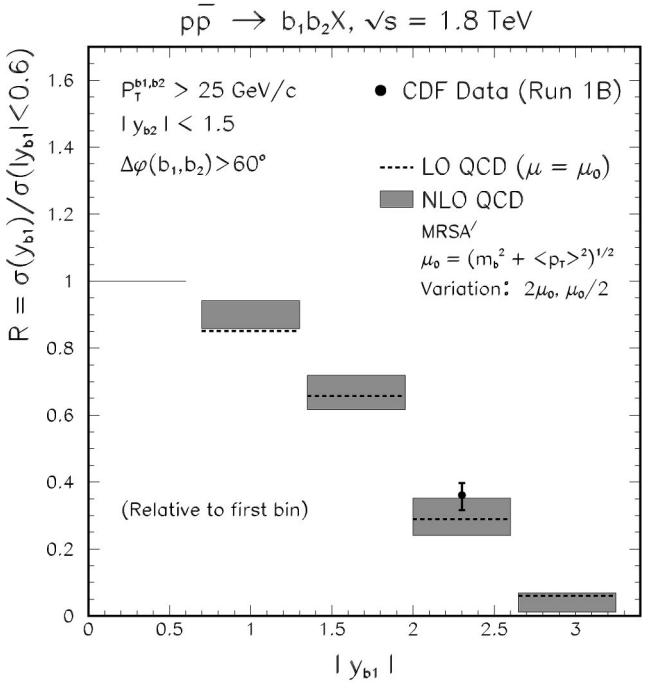

FIG. 16. The normalized rapidity distribution of the trigger b quark. Filled boxes are the theory prediction in each bin taking into account variations in the scale, the dashed line is the LO result, and the experimental measurement is indicated by the error bar.

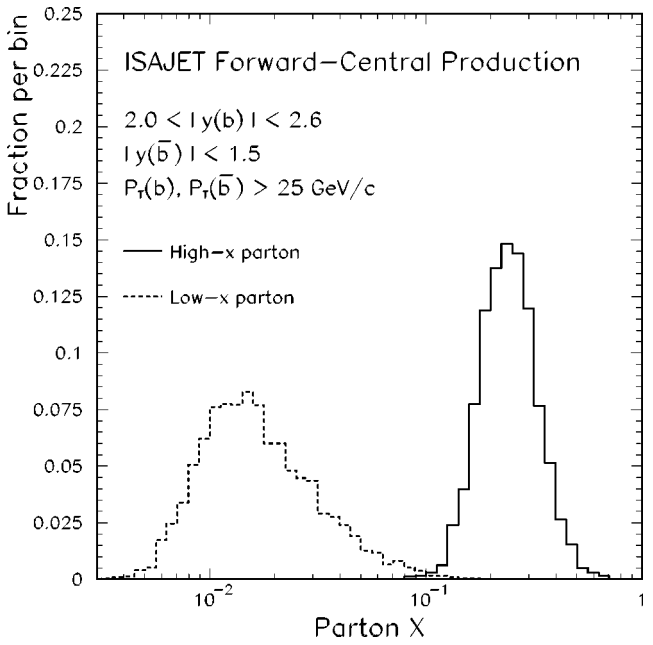

FIG. 17. The fraction of hadron momentum carried by the colliding partons in ISAJET forward-central $b\bar{b}$ production. The high-x parton corresponds to Eq. (4) [(5)] when y_b is positive (negative).

recent studies which modify the heavy quark fragmentation function [12] or employ a variable flavor-number perturbative calculation [13].

As mentioned in Sec. I, the shape of the rapidity distribution at large y is sensitive to the gluon distribution in the proton at large x. Assuming leading order ($2\rightarrow 2$) kinematics, the range of x values probed by this measurement can be estimated using the following equations,

$$x_1=\frac{M_T}{\sqrt{s}}[e^{+y_b}+e^{+y_{\bar{b}}}] \tag{4}$$

$$x_2=\frac{M_T}{\sqrt{s}}[e^{-y_b}+e^{-y_{\bar{b}}}] \tag{5}$$

where $M_T=\sqrt{m_b^2+p_T^2}$, and $\sqrt{s}$ is the center-of-mass energy of the colliding hadrons. In Fig. 17, we plot the fraction of proton momentum carried by the colliding partons in ISAJET forward-central $b\bar{b}$ events satisfying our cross section definition, where the x values were calculated using the generated b and $\bar{b}$ rapidities. The initial-state parton traveling in the direction of the forward b quark has momentum in the range $0.1<x<0.7$, while the second parton has momentum in the range $0.005<x<0.1$. Thus, the measurement is sensitive to $G(x,Q^2)$ in the region where it is not currently well constrained ($x>0.15$).

In Fig. 18, we show the gluon-gluon luminosity $G(x_1)G(x_2)$ as a function of y_b for a representative set of PDFs: MRSR2 (dashed) [45], CTEQ4HJ (dotted) [46], and MRS-Thorne (MRST) (dot-dash) [47], all normalized to the MRSA′ gluon distribution. The approximate correspondence between the momentum fraction of the high-x parton and the

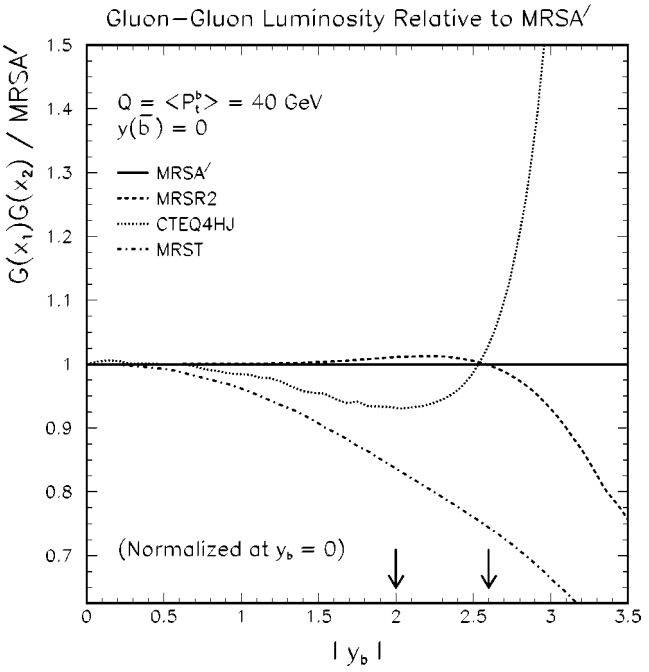

FIG. 18. Comparison of the gluon-gluon luminosity for MRSR2, CTEQ4HJ, and MRST PDFs, relative to MRSA′, as a function of $|y_b|$. Here we set $y_{\bar{b}}=0$ and $Q=40$ GeV. The curves are divided by MRSA′ and normalized to unity at $y_b=0$. Arrows indicate the approximate region covered by our measurement.

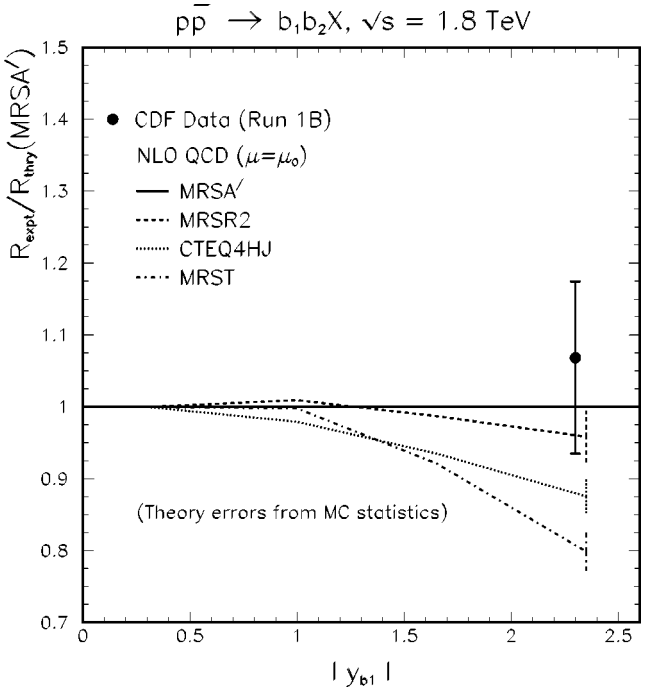

FIG. 19. Comparison of the ratio $R=\sigma(|y_{b_1}|)/\sigma(|y_{b_1}|<0.6)$ between data and theory using MRSA′ parton distribution functions. Theory curves for MRSR2, CTEQ4HJ, and MRST are divided by MRSA′ and normalized to unity in the first bin. Theory error bars are the statistical uncertainty from Monte Carlo integration, while the data error is combined statistical and systematic.

rapidity of the forward b quark is facilitated by setting $y_{\bar{b}}=0$ and $Q=40$ GeV in Eqs. (4) and (5), where the Q value is approximated by the mean p_T of b quarks in our data as determined by ISAJET. To simulate the cross section ratio measurement, all of the curves are normalized to unity at $y_b=0$. The approximate region sampled by this measurement is indicated by the arrows.

The comparison in Fig. 18 shows significant differences between the various gluon parameterizations, which arise from the different constraints used in the global fits. The MRSR2 PDFs are an updated version of the MRSA′ ''best fit'' parameterization, using more recent HERA data and a value of α_s more consistent with the world average, and there is little difference between the two gluon distributions. In contrast, the CTEQ4HJ gluon distribution was specifically designed to fit the high-E_T jet data measured by CDF using Run 1A (1992–1993) data [48]. The result is a rapid rise at high x, or equivalently, large rapidity. Since the total momentum carried by gluons is well constrained, the increase at large x must be accompanied by a decrease at lower momentum fraction, which happens to occur in the region sampled by this measurement. The MRST parton set represents the first systematic attempt to include k_T smearing when fitting prompt photon data as part of a global parton distribution analysis. They obtain three different parametrizations corresponding to a range of $\langle k_T\rangle$ from 0.0 to a maximum value consistent with data. Since a larger $\langle k_T\rangle$ is compensated by a smaller gluon distribution, the three parameterizations are referred to as MRST($g\uparrow$), MRST, and MRST($g\downarrow$). We show in Fig. 18 the MRST gluon distribution, which is significantly smaller than MRSA′ in the region dominated by prompt photon data. The MRST($g\uparrow$) gluon distribution (not shown) includes no k_T smearing and is consistent with MRSA′, while MRST($g\downarrow$) is approximately 60% lower than MRSA′ at $y_b=2.0$. The CTEQ4M [46] gluon distribution (not shown) is a best-fit parameterization similar to MRSA′ and MRSR2.

In Fig. 19, we compare the measured cross section ratio with the NLO QCD predictions using the PDFs described above. To better discern the differences between the various theory curves, we present the results in the format data/theory, where our data point and the theory curves are divided by the result using MRSA′. The vertical error bars at the end of each theory curve indicate the statistical uncertainty from the Monte Carlo integration; we do not include the variation with scale in this plot. The measurement error is combined statistical and systematic.

As suggested by the comparison in Fig. 18, we find good agreement between data and QCD using the MRSR2 PDFs, while the CTEQ4HJ and MRST results are lower by approximately 1.5 and 2.0σ, respectively, where σ is the total error on the measurement. We note that taking an extreme value of the Peterson fragmentation parameter, $\epsilon=0$, for both central and forward production, would decrease $R_{\rm expt}$ by 15% (Sec. VI A), and bring our result into agreement with the CTEQ4HJ prediction and within 1σ of the MRST result. It is interesting that the differences between PDF sets, which are compatible with all existing data on large-x gluons, are as large as the uncertainty of our present measurement. This suggests that with more statistics, the study of rapidity cor-

relations in $b\bar{b}$ production will become an important input in constraining the large-x gluon distributions. To this goal, an extended reach in rapidity for the forward b quark would explore a region of the gluon luminosity where differences between various PDF sets are more marked (see Fig. 18).

VII. CONCLUSIONS

We have presented the first direct measurement of $b\bar{b}$ rapidity correlations at a hadron collider. Using forward and central high-p_T muon triggers, two independent samples were accumulated corresponding to events enriched in forward and central b decays, respectively. In each sample a secondary vertex b-tagging algorithm was used to identify a central recoil jet likely to contain a heavy quark. The fraction of events in each sample due to $b\bar{b}$ production was determined by simultaneously fitting p_T^{rel} between the muon and μ jet, and the transverse decay length of the b-tagged jets.

We have measured the ratio of forward to central $b\bar{b}$ production and find $R_{\mathrm{expt}}=0.361\pm0.033^{+0.015}_{-0.031}$, where the first uncertainty is statistical and the second is systematic. This result is in good agreement with the NLO QCD prediction using MRSA′ PDFs, $R_{\mathrm{theor}}=0.338^{+0.014}_{-0.097}$. We find no evidence of anomalous forward B production, as allowed by recent studies which modify the heavy quark fragmentation function [12] or employ a variable flavor-number perturbative calculation [13]. A comparison with the QCD result using MRSR2 also shows good agreement. The predictions using CTEQ4HJ and MRST disagree with our measurement at the 1.5 and 2.0σ level respectively; however, this level of disagreement is comparable to the large (15%) estimated uncertainty when taking the extreme value of the Peterson fragmentation parameter, $\epsilon=0$. Given the small number of measurements directly sensitive to the gluon distribution at high x, this result represents an important additional constraint that could reduce the range of possible gluon parametrizations once a better understanding of the fragmentation process is achieved.

ACKNOWLEDGMENTS

We thank the Fermilab staff and the technical staff at the participating institutions for their essential contributions to this research. This work is supported by the U.S. Department of Energy and the National Science Foundation, the Natural Sciences and Engineering Research Council of Canada, the Istituto Nazionale di Fisica Nucleare of Italy, the Ministry of Education, Science and Culture of Japan, the National Science Council of the Republic of China, and the A. P. Sloan Foundation.

[1] The rapidity of the b quark y_b is defined to be $\frac{1}{2}\ln[(E+p_z)/(E-p_z)]$, where E is the energy and p_z is the longitudinal momenta of the b quark.
[2] UA1 Collaboration, C. Albajar *et al.*, Phys. Lett. B **256**, 121 (1991).
[3] CDF Collaboration, F. Abe *et al.*, Phys. Rev. Lett. **71**, 500 (1993); **71**, 2396 (1993); **75**, 1451 (1995).
[4] DØ Collaboration, S. Abachi *et al.*, Phys. Rev. Lett. **74**, 3548 (1995).
[5] UA1 Collaboration, C. Albajar *et al.*, Z. Phys. C **61**, 41 (1994).
[6] CDF Collaboration, F. Abe *et al.*, Phys. Rev. D **53**, 1051 (1996); **55**, 2546 (1997).
[7] DØ Collaboration, S. Abachi *et al.*, in *DPF '96*, Proceedings of the Division of Particles and Fields of the APS, Minneapolis, Minnesota, edited by K. Heller, J. K. Nelson, and D. Reeder (World Scientific, Singapore, 1996), p. 839, hep-ex/9905024.
[8] P. Nason, S. Dawson, and R.K. Ellis, Nucl. Phys. **B303**, 607 (1988); **B327**, 49 (1989); **B335**, 260(E) (1990).
[9] W. Beenakker, H. Kuijf, W.L. van Neerven, and J. Smith, Phys. Rev. D **40**, 54 (1989); W. Beenakker, W.L. van Neerven, R. Meng, G.A. Schuler, and J. Smith, Nucl. Phys. **B351**, 507 (1991).
[10] M. Mangano, P. Nason, and G. Ridolfi, Nucl. Phys. **B373**, 295 (1992).
[11] S. Frixione *et al.*, in *Heavy Flavours II*, Advanced Series on Directions in High-Energy Physics, edited by A. J. Buras and M. Lindner (World Scientific, Singapore, 1998), p. 609.
[12] M. Mangano, lectures given at the International School of Physics, ''Enrico Fermi'': Heavy Flavor Physics—A Probe of Nature's Grand Design, Varenna, Italy, 1997, hep-ph/9711337.
[13] F.I. Olness, R.J. Scalise, and Wu-Ki Tung, Phys. Rev. D **59**, 014506 (1999).
[14] DØ Collaboration, S. Abachi *et al.*, XXIX International Conference on High Energy Physics—ICHEP98, 1998, Vancouver, B.C., Canada, hep-ex/9907019.
[15] E.L. Berger, Phys. Rev. D **37**, 1810 (1988).
[16] CTEQ Collaboration, J. Huston *et al.*, Phys. Rev. D **58**, 114034 (1998).
[17] CDF Collaboration, F. Abe *et al.*, Nucl. Instrum. Methods Phys. Res. A **271**, 387 (1988), and references therein.
[18] D. Amidei *et al.*, Nucl. Instrum. Methods Phys. Res. A **350**, 73 (1994).
[19] P. Azzi *et al.*, Nucl. Instrum. Methods Phys. Res. A **360**, 137 (1995).
[20] F. Bedeschi *et al.*, Nucl. Instrum. Methods Phys. Res. A **268**, 50 (1988).
[21] G. Ascoli *et al.*, Nucl. Instrum. Methods Phys. Res. A **268**, 33 (1988).
[22] K. Byrum *et al.*, Nucl. Instrum. Methods Phys. Res. A **268**, 46 (1988).
[23] L. Balka *et al.*, Nucl. Instrum. Methods Phys. Res. A **267**, 272 (1988); S. Bertolucci *et al.*, *ibid.* **267**, 301 (1988); Y. Fukui *et al.*, *ibid.* **267**, 280 (1988); G. Brandenburg *et al.*, *ibid.* **267**, 257 (1988); S. Cihangir *et al.*, *ibid.* **267**, 249 (1988).
[24] CDF Collaboration, F. Abe *et al.*, Phys. Rev. D **45**, 1448 (1992).
[25] CDF Collaboration, F. Abe *et al.*, Phys. Rev. D **47**, 4857 (1993).

[26] CDF Collaboration, F. Abe *et al.*, Phys. Rev. Lett. **68**, 1104 (1992).
[27] D. Amidei *et al.*, Nucl. Instrum. Methods Phys. Res. A **269**, 51 (1988); J.T. Carroll *et al.*, *ibid.* **263**, 199 (1988).
[28] G.W. Foster *et al.*, Nucl. Instrum. Methods Phys. Res. A **269**, 93 (1988).
[29] CDF Collaboration, F. Abe *et al.*, Phys. Rev. D **50**, 2966 (1994).
[30] CDF Collaboration, F. Abe *et al.*, Phys. Rev. D **58**, 072001 (1998).
[31] A. Warburton, Ph.D. thesis, University of Toronto, 1998.
[32] F. Paige and S. D. Protopopescu, BNL Report No. 38034, 1986.
[33] A. Martin *et al.*, Phys. Lett. B **354**, 155 (1995).
[34] C. Peterson *et al.*, Phys. Rev. D **27**, 105 (1983).
[35] J. Chrin, Z. Phys. C **36**, 165 (1987); ALEPH Collaboration, D. Buskulic *et al.* Phys. Lett. B **244**, 551 (1990).
[36] P. Avery, K. Read, and G. Trahern, Cornell Internal Note No. CSN-212, 1985.
[37] V. Barger, A. Stange, and R. Phillips, Phys. Rev. D **44**, 1987 (1991).
[38] J. Olsen, Ph.D. thesis, University of Wisconsin, 1998.
[39] CDF Collaboration, F. Abe *et al.*, Phys. Rev. Lett. **76**, 3070 (1996).
[40] Particle Data Group, C. Caso *et al.*, Eur. Phys. J. C **3**, 1 (1998).
[41] OPAL Collaboration, G Alexander *et al.*, Phys. Lett. B **364**, 93 (1995); Z. Phys. C **67**, 27 (1995).
[42] ALEPH Collaboration, D Buskulic *et al.*, Phys. Lett. B **357**, 699 (1995).
[43] M. Cacciari and M. Greco, Phys. Rev. D **55**, 7134 (1997).
[44] CDF Collaboration, F. Abe *et al.*, Phys. Rev. D **60**, 051101 (1999).
[45] A.D. Martin, R.G. Roberts, and W.J. Stirling, Phys. Lett. B **387**, 419 (1996).
[46] CTEQ Collaboration, H.L. Lai *et al.*, Phys. Rev. D **55**, 1280 (1997).
[47] A.D. Martin, R.G. Roberts, W.J. Stirling, and R.S. Thorne, Eur. Phys. J. C **4**, 463 (1998).
[48] CDF Collaboration, F. Abe *et al.*, Phys. Rev. Lett. **77**, 438 (1996).